Journal of Hazardous Materials 399 (2020) 122935

Contents lists available at ScienceDirect

Journal of Hazardous Materials

journal homepage: www.elsevier.com/locate/jhazmat

Mineralogy, geochemistry and toxicity of size-segregated respirable deposited dust in underground coal mines

Pedro Trechera[a,b,*], Teresa Moreno[a], Patricia Córdoba[a], Natalia Moreno[a], Xinguo Zhuang[c], Baoqing Li[c], Jing Li[c], Yunfei Shangguan[c], Konrad Kandler[d], Ana Oliete Dominguez[e], Frank Kelly[e], Xavier Querol[a,c]

[a] Institute of Environmental Assessment and Water Research (IDAEA-CSIC), 08034 Barcelona, Spain
[b] Department of Natural Resources and Environment, Industrial and TIC Engineering (EMIT-UPC), 08242, Manresa, Spain
[c] Key Laboratory of Tectonics and Petroleum Resources, China University of Geosciences, Ministry of Education, Wuhan, 430074, China
[d] Institute of Applied Geosciences, Technical University Darmstadt, 64287, Darmstadt, Germany
[e] MRC-PHE Centre for Environment and Health, King's College London, London, SE1 9NH, UK

GRAPHICAL ABSTRACT

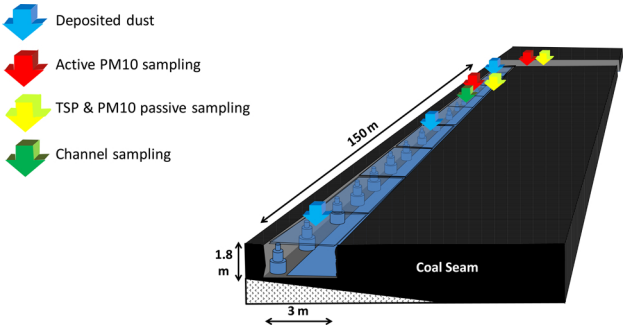

ARTICLE INFO

Editor: Rinklebe Jörg

Keywords:
Coal mining dust
Occupational exposure
Toxicology
Chemistry
China

ABSTRACT

We focus on a comparison of the geochemistry and mineralogy patterns found in coal, deposited dust (DD), respirable deposited dust (RDD) and inhalable suspended dust (PM10) from a number of underground mines located in China, with an emphasis on potential occupational health relevance. After obtaining the RDD from DD, a toxicological analysis (oxidative potential, OP) was carried out and compared with their geochemical patterns. The results demonstrate: i) a dependence of RDD/DD on the moisture content for high rank coals that does not exist for low rank coals; ii) RDD enrichment in a number of minerals and/or elements related to the parent coal, the wear on mining machinery, lime gunited walls and acid mine drainage; and iii) the geochemical patterns of RDD obtained from DD can be compared with PM10 with relatively good agreement, demonstrating that the characterization of DD and RDD can be used as a proxy to help evaluate the geochemical patterns of suspended PM10. With regards to the toxicological properties of RDD, the Fe content and other by-products of pyrite oxidation, as well as that of anatase, along with Si, Mn and Ba, and particle size (among others), were highly correlated with Ascorbic Acid and/or Glutathione OP.

* Corresponding author.
E-mail address: pedro.trechera@idaea.csic.es (P. Trechera).

https://doi.org/10.1016/j.jhazmat.2020.122935
Received 19 December 2019; Received in revised form 14 April 2020; Accepted 11 May 2020
Available online 25 May 2020

1. Introduction

Coal mining and its associated environmental impact, including exposure to coal mine dust, remain high on the list of global health issues to be ameliorated. The main impacts of coal mining activities result from emissions of atmospheric pollutants, with implications for both climate change and air quality. While the climatic effects arise from the increased emissions of greenhouse pollutants associated with mining activities and deforestation, the problems linked to air quality are largely associated with the local dust emissions created by mining work, waste disposal, coal/waste fires, the transport and handling of coal and the increases in population and industry around mining areas (Aneja et al., 2012; Duarte et al., 2019; Fabiano et al., 2014; Ghose and Majee, 2007; Hendryx et al., 2008; Patra et al., 2016; Petavratzi et al., 2005; Rout et al., 2014; Tang et al., 2017; Visser, 1992).

In underground coal mining, dust emissions are much higher in the working front (WF) galleries, where coal is being worked via shearers, drilling and other mining operations, despite the ventilation systems and the common use of water spraying (Colinet et al., 2010; Li et al., 2019; Moreno et al., 2019). Dust levels decrease from the WFs to the coal extraction galleries (with continuous belts) and access galleries (usually much better ventilated). Other sources of underground dust include the resuspension of deposited coal dust and wear on machinery (mining machinery, coal and gangue extraction belts and worker transport systems) during ventilation. Furthermore, on the surface, waste disposal, coal milling and handling, and the transport of coal and gangue can be significant sources of dust if containment measures are not properly implemented.

In open pit coal mines, many of the same sources of coal mine dust are present; however, compared to underground coal mines, there is higher dispersion, which is commonly offset by much higher volumes of coal and gangue (and accordingly higher emissions) and the large number of heavy trucks that enhance widespread resuspension and contribute exhaust emissions. Another air quality hazard associated with mining is occasional coal or waste fires, which can occur in open pits, underground mines and waste dumps (Haibin and Zhenling, 2010; Pallarés et al., 2017; Querol et al., 2008) and produce significant amounts of associated PM and gaseous pollutant emissions (Jiang et al., 2014; Kim, 2004; O'Keefe et al., 2010; Querol et al., 2011).

The potential impact of coal and gangue dust on human health and ecosystems can vary widely according to the grain size and mineralogical and chemical composition (Borm, 1997; Li et al., 2017; Sarver et al., 2019) of the particulates being inhaled. Obviously, the finer the dust, the deeper it can penetrate into the respiratory system, with the $< 4\,\mu m$ dust fraction accepted widely as the respirable dust fraction (Brown et al., 2013; Gustafsson et al., 2018; Johann-Essex et al., 2017). The higher this fraction is in the coal dust, especially if rich in crystalline silica and/or metals, the higher the potential cell inflammation and consequent health damage (Brodny and Tutak, 2018; Castranova, 2000; Cohen et al., 2008; Ercal et al., 2001; Ghio and Madden, 2017; Niosh, 2002; Schins and Borm, 1999; Valko et al., 2016).

Research from last decades on the toxicology of air pollution has identified oxidative stress as a unifying feature underlying the toxic actions of the air pollutants that cause concern (Kelly, 2003). Thus, it is now well accepted that pulmonary inflammation caused by exposure to air pollution is induced via oxidant signalling pathways. Classical studies on residual oil fly ash and urban PM evidenced that a high concentration of metals, such as, Fe, Ni, and V, can lead to aldehyde generation, pulmonary inflammation and oxidative stress, which correlates with the Fe content of these particles (Costa and Dreher, 1997; Kadiiska et al., 1997). Newer studies on Fe-ore PM also point to the high impact of Fe in the oxidative potential (OP) of PM (Soltani et al., 2018), with exceptions, such as subway PM (Moreno et al., 2017). Thus, the mode of occurrence of Fe and other metals in PM also seems to have a large impact on the OP. Furthermore, organic pollutants, such as PAH, might contribute significantly to increasing this oxidative stress (Chuang et al. (2013) and Kelly (2003), among others).Although much has been written on the problem of worker exposure to coal dust, there remain few data on the mineralogy, chemistry and toxicology of inhalable-sized dust samples collected directly from inside mines. In this context, the purpose of this study is to characterize coal mine dust from diverse areas in four different underground coal mines located in Southwest, South and North China, with the aim of evaluating dust particle sizes, mineralogical and geochemical patterns and their potential impacts on health, as well as to identify source origins by combining geochemical, mineralogical and toxicological tools. We also investigate how dust deposited in coal mines can be used to predict the mineralogical and chemical patterns of respirable dust in the mine. We adopt a novel approach involving separating out the respirable component present in deposited dust and comparing compositional patterns in samples of total suspended ambient particles (TSP) and PM10 (Particulate Matter finer than 10 μm in diameter).

2. Methodology

2.1. Sampling

Fig. 1 and S1 to S4 and Tables 1 and 2 show the regional location, map of the mines and type and number of coal mine dust samples collected in an Anthracite North China (ANC), a Bituminous South China (BSC), a Bituminous South-West China (BWC) and a Sub-bituminous (SSC) underground mines. In the case of the ANC mine (Figs. 1 and S1), coal seam #2-1 (4.1 m thick), was being worked at the time of sampling. In the BSC mine (Figs. 1 and S2), coal seam #4-1 (1.2 m thick) was being worked, but the dust was collected in a WF that had been inactive for 2 years. In the case of the BWC mine (Figs. 1 and S3), coals seams #7 (1.8 m thick) and #11 (2.2 m thick) were being worked during our sampling campaign. Finally, in the case of the SSC mine (Figs. 1 and S4), coal seam D-3 (2.0 m thick) was being worked. In all cases, deposited dust (DD) was collected in different parts of each mine, and worked coal was also sampled by means of channel profile (CP) samples at the WF galleries in order to compare the chemical compositions of the dust and parent coal in the same WF.

The majority of samples analysed in this study consist of DD in different locations in the coal mines (Figs S1–S4). The sampling time was limited to around 4 − 6 h, although for logistic reasons this was reduced to just 1.5 h in the seam head face. Deposited dust was collected either in plastic trays (left for 1 − 2 hours in zones of high concentrations such as WF galleries) or, more commonly, using brushes, and later stored in plastic bags. In addition, in the BWC mine we collected underground ambient PM samples finer than 10 μm and in the

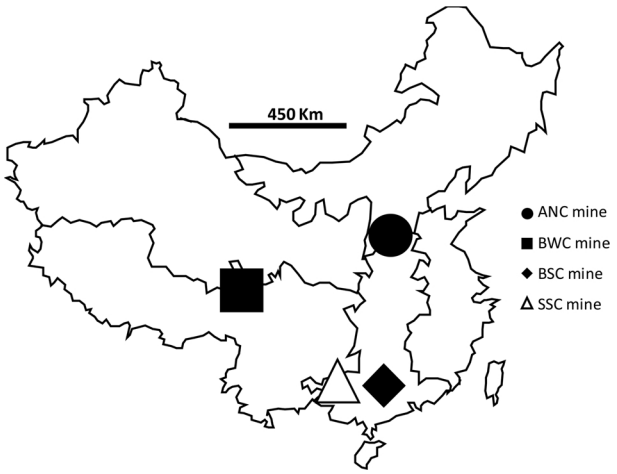

Fig. 1. Location of all the underground coal mines sampled in Democratic Republic of China.

Table 1
Samples of deposited dust on the ground (DD) and respirable deposited dust (RDD, < 4 μm) from the four underground mines. WF, Working front; GW, Gunited walls; FTW, Floor of train wagons.

Mine	Location	Type of sample
Bituminous South-West	GW #7	DD
Bituminous South-West	GW #7	DD
Bituminous South-West	GW #11	DD
Bituminous South-West	GW #11	DD
Bituminous South-West	1000 m WF #7	DD
Bituminous South-West	900 m WF #7	DD
Bituminous South-West	300 m WF #7	DD
Bituminous South-West	200 m WF #7	DD
Bituminous South-West	100 m WF #7	DD
Bituminous South-West	50 m WF #7	DD
Bituminous South-West	15 m WF #7	DD
Bituminous South-West	Workers rest #7	DD
Bituminous South-West	WF #7	DD
Bituminous South-West	WF #7	DD
Bituminous South-West	WF #11	DD
Bituminous South-West	WF #11	DD
Bituminous South-West	Wall drilling front #11	DD
Bituminous South-West	Wall drilling front #11	DD
Bituminous South-West	FTW	DD
Bituminous South-West	Coal mill	DD
Bituminous South-West	Coal mill	DD
Bituminous South-West	Coal gangue	DD
Bituminous South-West	Coal gangue	DD
Bituminous South-West	Production coal	DD
Bituminous South-West	GW #7	RDD
Bituminous South-West	300 m WF #7	RDD
Bituminous South-West	100 m WF #7	RDD
Bituminous South-West	50 m WF #7	RDD
Bituminous South-West	WF #7	RDD
Bituminous South-West	WF #11	RDD
Bituminous South-West	Floor train wagons	RDD
Subbituminous South	2000 m D-3	DD
Subbituminous South	100 m D-3	DD
Subbituminous South	25 m D-3	DD
Subbituminous South	50 m D-3	DD
Subbituminous South	WF D-3	DD
Subbituminous South	Coal belt	DD
Subbituminous South	Coal mill	DD
Subbituminous South	2000 m D-3	RDD
Subbituminous South	100 m D-3	RDD
Subbituminous South	WF D-3	RDD
Subbituminous South	Coal mill	RDD
Bituminous South	100 m WF #4-1	DD
Bituminous South	50 m WF #4-1	DD
Bituminous South	100 m WF #4-1	RDD
Bituminous South	50 m WF #4-1	RDD
Anthracite North	Air shaft #2-1	DD
Anthracite North	Air shaft #2-1	RDD
Anthracite North	Air shaft #2-1	RDD

10–200 μm range (PM10 and PM10 − 200, respectively), using two CIP-10 Thoracic (CIP-10T) instruments. This device is used for the evaluation of risks associated with the exposure to hazardous environments where batteries cannot be used, such as underground coal mines, and to collect ambient dust at a rate of 7 L/min. The CIP-10T allows the collection of both PM10 coal dust on polyurethane foams, with a coarser dust fraction being brushed into the impactor zone. The third sampling method, also conducted in the BWC mine, involved using standard electron microscopy aluminium stubs covered with copper foil, which was then covered with glue. These were distributed at different locations within the mine (Fig. S3) to obtain suspended dust samples via dry deposition for scanning electron microscopy purposes. Finally, coal samples were collected at the coal face as primary source materials to allow comparisons with the deposited airborne dust samples obtained elsewhere in the mine.

Table 2
Samples from channel profiles (CP) collected at the working fronts of the different mines, suspended PM10 and PM10-200 from the BWC mine, and of suspended dust (SD) and respirable deposited dust (RDD) for Scanning Electron Microscope (SEM).

Mine	Location	Type of sample
Bituminous South-West	1.8 m profile #7	CP
Bituminous South-West	2.2 m profile #11	CP
Subbituminous South	2.3 m profile D-3	CP
Bituminous South	1.2 m profile #4 − 1	CP
Anthracite North	4.1 m profile #2 − 1	CP
Bituminous South-West	Train station to WF #7	SD CIP PM10
Bituminous South-West	Train station to WF #11	SD CIP PM10
Bituminous South-West	Train station to WF #7	SD CIP PM10 − 200
Bituminous South-West	Train station to WF #11	SD CIP PM10 − 200
Bituminous South-West	WF #7	CP_SEM
Subbituminous South	WF D-3	CP_SEM
Bituminous South-West	WF#7	SD_SEM
Bituminous South-West	WF#11	SD_SEM
Bituminous South-West	Gallery #7	SD_SEM
Subbituminous South	Gallery D-3	RDD_SEM

2.2. Particle size

A total of 34 deposited dust samples and five CP samples belonging to the four underground coal mines in China were analysed in order to characterize the underground coal dust patterns and interpret composition and origin. All deposited dust samples were sieved at 500 μm (to obtain DD samples, or deposited dust < 500 μm). The respirable deposited dust (RDD) samples were separated from a selection of 16 bulk DD samples using a PM2.5 and PM10 separator device (Moreno et al., 2005) that allows the collection of samples on 47 mm polycarbonate filters (0.60 μm pore size).

Particle size distributions of both DD and RDD samples were obtained using a Malvern Mastersizer. For DD samples, a Scirocco 2000 unit was coupled to get the particle sizes in dry conditions. Samples moved along the Scirocco 2000 system on a tray as oscillation and air pressure forced them to scatter into individual grains, getting them ready for sizing via laser diffraction. RDD samples (with very low sample volumes) particle size distribution was obtained using a wet (water-Polyphosphate RDD suspension) HydroG 2000 coupled unit (Sperazza et al., 2004).

2.3. Mineralogical and morphological characterization

The mineralogical analyses of CP, DD and RDD samples were performed using a X-Ray Diffraction (XRD) Bruker D8 A25 Advance, θ-θ diffractometer with $CuK_{\alpha}1$ radiation, Bragg-Brentano geometry and a position-sensitive LynxEye detector. The diffractograms were obtained at 40 kV and 40 mA while scanning from 4° to 60° of 2θ, with a step size of 0.019° and a counting time of 0.1 s/step maintaining the sample's rotation (15/min). The crystalline phase identification was carried out using the EVA software package (Bruker), which uses the ICDD (International Centre for Diffraction Data) database. Semi-quantitative XRD analysis was performed via the method devised by Chung (1974) for the quantitative analysis of multi-component systems.

The scanning electron microscopes JEOL JSM-7001F and Quanta 400F ESEM with Oxford X-Max 150 EDX detector, both with secondary and backscattered electron detectors, at the University of Barcelona and Technical University of Darmstadt, respectively, were used to analyse samples prepared on copper-glue surfaces.

2.4. Proximate, ultimate and chemical characterization

Proximate and ultimate analyses of the CP and DD samples were performed using the ISO and ASTM recommendations (ISO-589, 1981; ISO-1171, 1976; ISO-562, 1974; ASTM D-3286, 1996). In order

Table 3
Size distribution and moisture (% air dried, ad) of all deposited dust (DD) samples in %wt (weight) and %v (volume). WF, Working front; GW, Gunited walls; FTW, Floor of train wagons. BWC, Bituminous South-West China; SSC, Subbituminous South China; BSC, Bituminous South China; and ANC, Anthracite North China.

Mine	Location	< 500 μm (%wt)	< 10 μm (%v)	< 4 μm (%v)	< 2.5 μm (%v)	M (%ad)
BWC	GW #7	80.62	23.30	13.07	7.96	0.87
BWC	GW #7	40.42	6.90	3.30	1.58	1.71
BWC	1000 m WF #7	48.05	11.97	4.67	2.22	0.74
BWC	GW #11	75.51	21.88	9.98	4.90	1.03
BWC	GW #11	89.00	26.86	13.55	7.51	1.03
BWC	1000 m WF #7	33.50	4.80	1.80	0.70	1.36
BWC	50 m WF #7	57.00	18.20	7.20	3.50	1.19
BWC	25 m WF #7	74.70	26.30	11.20	5.50	0.75
BWC	15 m WF #7	76.80	26.90	11.30	5.60	0.39
BWC	WF #7	92.50	30.60	12.80	6.20	0.38
BWC	WF #7	92.13	24.91	10.69	5.23	0.38
BWC	WF #11	94.76	29.19	12.50	6.05	0.21
BWC	WF #11	94.93	29.87	12.95	6.28	1.30
BWC	FTW	71.03	11.99	6.16	3.01	0.41
BWC	Coal mill	61.77	10.67	5.05	2.33	0.79
SSC	2000 m WF D-3	88.70	65.60	32.80	19.50	2.90
SSC	100 m WF D-3	84.70	57.50	32.60	20.30	1.86
SSC	50 m WF D-3	80.60	51.90	28.80	18.10	1.63
SSC	25 m WF D-3	79.50	46.50	25.00	15.70	1.41
SSC	WF D-3	87.90	38.70	21.20	13.50	1.67
SSC	Coal belt	29.70	12.00	6.70	4.40	1.94
SSC	Coal mill	87.00	21.80	10.80	6.70	2.40
BSC	50 m WF #4 − 1	96.10	53.20	25.30	14.70	0.98
BSC	100 m WF #4 − 1	95.70	57.70	27.70	16.10	0.64
ANC	Air shaft #2-1	77.68	43.76	19.10	9.52	0.97

determine moisture (M, at 105 °C) and ash yield (HTA, at 750 °C), the standard procedures, i.e., ASTM D3302M-17 for M and ASTM D3174-12 for HTA, were followed.

For CP, DD, RDD and PM10 (collected in the polyurethane foam provided in the CIP-10T devices) sample chemical analysis, a dried portion of the sample was acid-digested using a special two-step digestion method devised by Querol (1993) and Querol et al. (1997) to retain volatile elements. The concentrations of major elements in the acid digests were determined using Inductively-Coupled Plasma Atomic-Emission Spectrometry (ICP-AES, Iris Advantage Radial ER/S device from Thermo Jarrell-Ash). Trace elements were analysed by Inductively-Coupled Plasma Mass Spectrometry (ICP-MS, X-SERIES II Thermo Fisher Scientific, Bremen, Germany). Digestion of international reference materials (SARM19 and NIST SRM 1633b) and blanks were prepared following the same procedure.

After eleven repetitions of the analysis of the above reference materials, analytical errors were estimated to be within ± 1% of 7% for most major elements in both the SARM19 coal and NIST-1633b fly ash reference materials, with the exceptions of P in SARM19 (29%) and Na in the latter (10%, with relative standard deviations (RSDVs) ranging from 2% to 7%). The trace elements errors were in the range of ± 0 − 5% for Co (7%), U (7%), Cs (8%), Cu (10%), Zn (41%), Zr (31%) and Hf (14%) in SARM19 coal and ± 0 − 4% for all certified and 'for reference' elements in NIST-1633b-fly ash, with the exception of Sc (11%) and Ta (12%). The RSDVs were < 10% for most elements, with the exception of Li, Be, Sc, Cu, Se and Mo (11 − 20%) and Zr, Cd and Ta (21–58%) for SARM19 and < 10% for all elements, with the exception of Mo (14%), and Ta, Zr and Be (24–26%), for NIST-1633b. Because Si is lost during HF evaporation during the digestion of the samples during ICP-AES and ICP-MS analyses, 3 mg of each RDD and DD sample was loaded on Teflon© 47 mm filters using ethanol suspensions to determine the Si/Al concentrations by means of X Ray Fluorescence (XRF, Thermo Scientific ARL QUANT'X Energy-Dispersive X-Ray Fluorescence (EDXRF)). Subsequently, this Si/Al ratio was applied to the Al (ICP-AES determined) concentrations measured for each sample to obtain the Si concentrations. The above reference materials were also used to determine the accuracy of the Si/Al ratios.

2.5. Respirable crystalline silica (RCS)

In order to determine the RCS content in the RDD fractions, an RCS reference material (certified reference material BCR-066, quartz) was added in two rounds (to obtain three measurements of the quartz XRD intensity, the original was used, followed by the ones formed by the two additions) to a 0.1 g sub-sample of each RDD sample to determine RCS content by the addition method. This content was evaluated by means of the correlation between the concentration added and the intensity area obtained from the strongest quartz peak when using XRD.

2.6. Toxicology tests: oxidative potential (OP)

The oxidative stress of the RDD samples was determined via the OP method, which is based on the consumption of ascorbic acid (AA), urate (UA) and glutathione (GSH) antioxidants, as described in detail by Soltani et al. (2018). The OP method involves the resuspension of each RDD sample in ethanol and a 4 h incubation with a synthetic solution containing equi-molar concentrations of AA, UA and GSH. The consumption of AA, UA and GSH is determined by following the methodology developed by Baker et al. (1990) and Iriyama et al. (1984). In-house controls of PM-free, negative PM (M120, Cabot Corporation, USA) and positive PM (NIST1648a, urban particulate from NIST, USA) followed the same protocol for control purposes. The OP of the RDD samples was expressed as the percentage of consumption of each antioxidant with reference to the in-house, particle-free control. To obtain a metric for the oxidative potential, the data was expressed as OP per μg of PM (OP^{AA}/μg PM and OP^{GSH}/μg PM). Data for the individual antioxidants was also combined to provide a total OP value (OP^{TOTAL}/μg). All data obtained were correlated with elemental and mineral concentrations using the software StataCorp LLC (College Station, Texas, USA) version Stata/SE 15.1.

3. Results and discussion

3.1. Particle size

Table 3 and Fig. 2 demonstrate that the finest size distribution

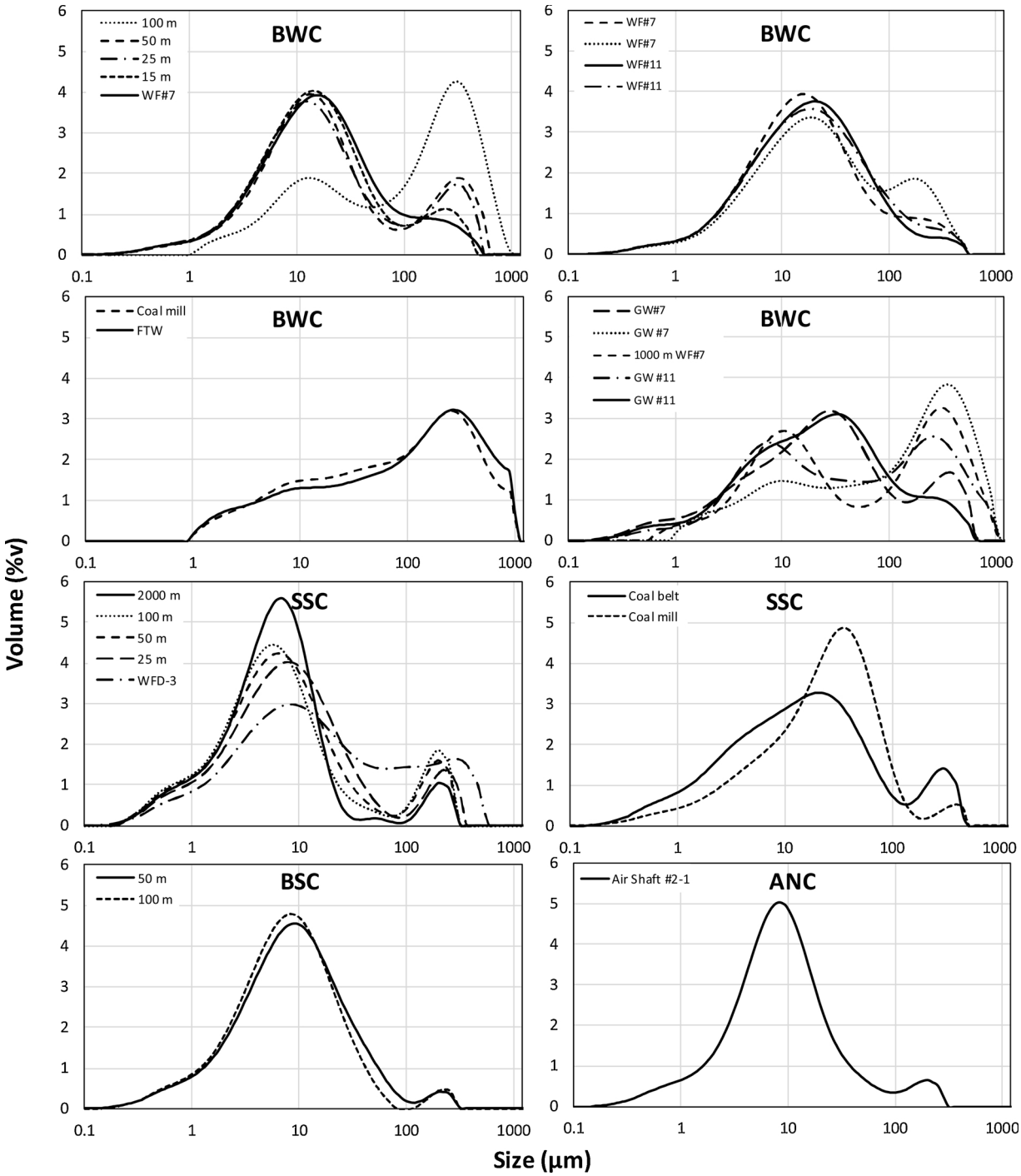

Fig. 2. Particle size distribution of the < 500 µm fraction of the deposited dust (DD) samples collected in the different underground coal mines. WF: Working front.

occurred in WFs samples (#7 and #11) which have 92–95%wt in the < 500 µm, and 25–31%v and 5–6%v in the < 10 µm and < 2.5 µm fractions, respectively. In the access galleries (1000m WF#7), an increase in the grain size was clearly evident within 15–100 m from the WF (95%wt to 28%wt, 27%v to 3%v and 4%v to 0.1%v for the above three fractions, respectively).

A number of galleries with walls covered in lime mortar (gunited walls) had a visually moderate level (markedly higher than the other access galleries but much lower than the WFs) of deposited fine dust (40–89%wt, 7–27%v, 3–14%v and 2–8%v for < 500 µm, < 10 µm, < 4 µm and 2.5 µm fractions, respectively).

The transition from the fine grain sizes in the WF and lime gunited galleries to the coarser grain sizes in the access galleries, train and coal mill is demonstrated clearly in the dry laser size distribution analyses presented in Fig. 2. In contrast, the particle size patterns of the DD from the underground subbituminous coal belonging to the SSC mine are characterised by an increase in the relative proportion allocated to the finest fractions as the distance to the WF increases, from 88%wt, 39%v and 14%v for the < 500 µm, < 10 µm and < 2.5 µm fractions at the WF, respectively, to 89%wt, 66%v and 20%v at a 2000 m distance. This change is attributed to the fact that close to the main emission sources (WF), the emissions of coarser particles are higher, and the finer fractions are transported further through the galleries. Obviously, the absolute concentrations of PM2.5 and PM10 are much higher closer to the

WF, but the relative contributions of these particles to the dust increase with the distance from the source. Furthermore, the DD close to the WF from the inactive BSC mine is characterised by a very high proportion of the finer fraction due to the lack of activity, reaching at 50 − 100 m from the WF 96%wt, 53 − 58%v and 15–16%v for the < 500 μm, < 10 μm and < 2.5 μm fractions, respectively.

The dust from the floor of train wagons and coal mills at the BWC mine is characterised by intermediate-sized particles (62–71%wt, 11–13%v and 2–3%v for < 500 μm, < 10 μm and < 2.5 μm fractions, respectively). As a comparison, the DD from the coal milling area at the SSC mine presents 87%wt, 22%v and 7%v for the < 500 μm, < 10 μm and < 2.5 μm fractions, respectively. The differences exhibited in these size proportions for the DDs from the mills, as suggested by visual observations, might be related to the high and low dust abatement control present in the BWC and SSC coal mills, respectively. Finally, the DD sample from the air shaft (air return) of the ANC mine is characterised by a fine particle size distribution, with 78%wt, 44%v and 10%v for the < 500 μm, < 10 μm, and < 2.5 μm fractions, respectively.

In the WFs of the mines, in addition to having much higher levels of DD (unquantified in our study, but visually very evident), the DD is markedly finer, with 11–13%v being in the respirable fraction (< 4 μm) in the BWC mine and 21%v being in that fraction in the SSC mine. Moving away from the WF, the rate of dust deposition decreases drastically in the BWC mine, and the respirable fraction reaches up to 7%v at 50 m. In the SSC mine, however, the respirable fraction increases to 29%v. In the case of the inactive BSC mine, the respirable fraction of the DD reaches up to 25–28%v at 50-100 m from the WF, while, in the coal mills, it accounts for 6–11%v (BWC and SSC, respectively, with high and low dust abatement controls). Dust from the floor of the wagons in the BWC mine contains a 5%v respirable fraction. In addition, the respirable size fraction distribution in the air return gallery of the ANC mine was 19%v.

In the case of the bituminous coal and anthracite DD samples (BWC and ANC mines), the particle size and the moisture content of the dust are markedly anti-correlated, even if moisture varied within a narrow range. Thus, the following regression equations were expressed for the three major size fractions (DD < 500 μm, < 10 μm and < 2.5 μm) based on 13 DD samples out of a total of 17 samples collected at both the ANC and BWC mines (most of the excluded samples are those from lime gunited galleries and train wagons):

$$DD500\ (\%wt < 500\,\mu m) = -37.75*Moisture\ (\%ad) + 97.26\ (R^2 = 0.79) \quad (1)$$

$$DD10\ (\%vol < 10\,\mu m) = -18.57*Moisture\ (\%ad) + 35.62\ (R^2 = 0.74) \quad (2)$$

$$DD2.5\ (\%vol < 2.5\,\mu m) = -4.18*Moisture\ (\%ad) + 7.67\ (R^2 = 0.73) \quad (3)$$

The correlations did not increase when the moist ash free basis was used (M,%maf, R^2 = 0.70, 0.67 and 0.66 for the three DD fractions, respectively) instead of the air dried moisture (M,%ad); no correlation was found between the fine dust proportions and ash yields (R^2 = 0.31, 0.19, 0.23, respectively, for DD500, DD10 and DD2.5).

In the active SSC coal mine, the anti-correlation between the moisture and the DD500, DD10 and DD2.5 fractions seen above is not apparent (Eqs. (4)–(6)), possibly due to the fact that in the ANC and BWC mines, the anthracite and bituminous ranks account for the low moisture in the coal or the total moisture might be highly influenced by condensation, while, in the subbituminous coal rank of the SSC, the moisture content of the dust seems to be dominated by the coal moisture. In this mine, it was observed that the ash content increases inversely with the moisture and the finer fractions of the DD, which should mean that, with a low correlation, the fine dust fractions decrease with increasing mineral matter in the dust. Thus, the following regression equations were obtained for the three major size fractions based on five of the seven samples collected:

$$DD500\ (\%wt < 500\,\mu m) = +5.06*Moisture\ (\%ad) + 74.68\ (R^2 = 0.51) \quad (4)$$

$$DD10\ (\%vol < 10\,\mu m) = +13.98*Moisture\ (\%ad) + 25.50\ (R^2 = 0.63) \quad (5)$$

$$DD2.5\ (\%vol < 2.5\,\mu m) = +2.51*Moisture\ (\%ad) + 12.66\ (R^2 = 0.28) \quad (6)$$

$$DD500\ (\%wt < 500\,\mu m) = -0.23*Ash\ yield\ (\%db) + 99.69\ (R^2 = 0.25) \quad (7)$$

$$DD10\ (\%vol < 10\,\mu m) = -0.80*Ash\ yield\ (\%db) + 106.29\ (R^2 = 0.52) \quad (8)$$

$$DD2.5\ (\%vol < 2.5\,\mu m) = -0.12*Ash\ yield\ (\%db) + 25.21\ (R^2 = 0.15) \quad (9)$$

No correlation analysis was performed with the DD samples since the BSC coal mine from which these samples came is abandoned, which could lead to uncertainties in relation to the moisture patterns of the other DD samples.

3.2. Mineralogy of deposited dust (DD)

Tables S1 and S2 list the mineralogical composition of all the samples collected in this study. The mineral compositions of the < 500 μm fractions of the DD samples from the BWC mine's WFs #7 and #11 are very different from each other but, as expected, very similar to those of their parent coal seams. The minerals present in the DD from WF #7 are clay minerals (19–23%, kaolinite-clinochlore, muscovite-illite), quartz (18–24%), carbonates (9–15%, calcite, siderite and ankerite), anatase (3 − 5%), pyrite (3–4%) and gypsum (< 1%). The parent coal is characterised by a lower mineral content: clay minerals (10%, kaolinite-clinochlore), quartz (13%), carbonates (4%, calcite and ankerite), anatase (2%), pyrite (2%) and feldspar (< 0.1%, albite-anorthite).

The DD from WF #11 is markedly lower in mineral matter, especially in quartz and pyrite, with 11–13% in clay minerals (muscovite-illite and kaolinite-clinochlore), 3–4% in carbonates (calcite and siderite) and 1% in quartz. The parent coal has a very similar composition, with 12% in clay minerals (muscovite-illite and kaolinite-clinochlore), 3% in carbonates (calcite and siderite), < 0.1% in anatase and < 0.1% in pyrite.

The DD from the SSC mine's WF is markedly different from that from the BWC mine, with higher contents of quartz (34%) and clays (37%, kaolinite-clinochlore and muscovite-illite), traces of feldspar (< 0.5%, albite-anorthite and microcline), anatase (< 0.5%), calcite (< 0.5%), gypsum (< 0.5%) and pyrite (< 1%). The CP of the coal seam worked at the SSC mine has a lower quartz content (12%) and a higher amount of clay (48%, kaolinite-clinochlore and muscovite-illite) than that of the DD collected in the WF.

In the inactive BSC mine, the DD samples collected only at 50 and 100 m from the WF had very similar mineralogy, with 30–33% clays (muscovite-illite and kaolinite-clinochlore), 5–6% quartz, 1–4% calcite, 3% gypsum and traces of pyrite, feldspar (albite-anorthite and microcline) and anatase. The worked coal seam here has slightly higher clay content (45%), plus trace calcite, anatase, pyrite, gypsum and quartz.

Deposited dust from the access galleries for the WFs #7 and #11 is characterised by the occurrence of gypsum and jarosite-alunite (up to 20% and 1%, respectively). These minerals usually occur in coal mining as weathering products of Fe-sulphides such as alunite (Cogram, 2018; Murphy et al., 2009; Welch et al., 2008) and might imply the enrichment of dust in hazardous elements, such as Pb, Zn, Cd and As, trapped by these minerals during their precipitation in acid mine drainages (AMDs), which might affect miners' exposure to toxic metals (Alcobe et al., 2001; Hudson-Edwards et al., 2008; Kerolli-Mustafa et al., 2015;

Kolitsch and Pring, 2001; Smith et al., 2006). In contrast, the galleries leading out from #7 and #11 that had walls gunited with lime mortar were characterised by very high calcite content (40–82%), probably due to the carbonation of lime (CaO), plus clays (2–24%, kaolinite-clinochlore and muscovite-illite), quartz (3–30%), anatase (< 1–6%) and sulphides (1–3%; pyrite). Moreover, the DD from the SSC access gallery (25 – 100 m from the WF) has a similar mineralogy to that of the WF DD, dominated by clays (28–41 vs. 37%) and quartz (30–38 vs 34%). The sample from the access gallery at 2000 m had somehow lower quartz content (19%) and a slightly higher content of gypsum (1%) when compared with the DD from the WF.

The DD from the BWC train wagons is characterised by high calcite (35%), whereas in the coal and gangue belts of the SSC mine is characterised by a high quartz content (40%) and low clay content (17%). On the other hand, the DD samples from coal milling have a slightly higher clay content (17% in the BWC mine, 24% in the SSC mine) and a slightly lower quartz content (9% in the BWC mine) than their respective coal CPs.

Finally, the DD from the ANC air shaft is highly enriched in calcite (27%), probably from lime gunited walls, with lower clay content (9%) (muscovite-illite and kaolinite-clinochlore), quartz (7%) and traces of pyrite and gypsum. This DD is characterised by the highest coal and lowest mineral content of all the samples analysed.

In the BWC mine, the occurrence of jarosite-alunite in the DD from the non-gunited access galleries and of gypsum in the gunited ones is very interesting. In coal mining, jarosite-alunite sulphates arise from coal-pyrite weathering, which produces sulphuric (H_2SO_4) acid and Fe^{2+} that subsequently yield to the jarosite-alunite precipitation at pHs below 3.7 (Murphy et al., 2009; Welch et al., 2008). In addition, the interaction of acidic sulphate with lime and/or calcite leads to the formation of gypsum. Fig. 3 summarises the relevant formation stages yielding the jarosite-alunite in mine dust in the access galleries (mechanism i). Thus, in the first formation pathway, the original gallery is cut into the fresh coal seam, inducing cracks and fractures in the coal seam and coal-bearing strata (Fig. 3a and b). Hence, the underground water can then access these seams via this fissure system, causing the weathering of the sulphide minerals and producing acidic acid mine waters that drain towards the surface of the gallery walls (Fig. 3c), where water evaporation causes the precipitation of jarosite-alunite crusts (in non- gunited galleries) or gypsum (in the lime gunited galleries) (Fig. 3d or e). Next, air flows from ventilation cause the break-up and airborne suspension of jarosite-alunite and/or gypsum-rich particles, which are subsequently deposited (Fig. 3f or g). Other possible mechanisms for the occurrence of jarosite-alunite in the mine dust include: ii) AMD solutions reach the roofs and walls of the galleries and produce a kind of acid rain that results in the formation of jarosite-alunite from the weathering of the pyrite of the DD; iii) water from the roofs and walls and from condensation causes the oxidation of DD containing pyrite, generating jarosite-alunite; and iv) the coal seam being worked is partially weathered and contains previously existing jarosite-alunite from epigenetic reactions of acid or from the weathering favoured by the local tectonic setting. The geochemical analyses (see below) should help to elucidate the main mechanism of jarosite-alunite formation. If jarosite-alunite-enriched metals (As, Sb) are also enriched in the DD, the formation mechanism illustrated in Fig. 3 is likely to prevail because these metals are usually enriched in AMD waters (He et al., 2019; Madzivire et al., 2019; Mohanty et al., 2018).

3.3. Geochemistry of coal and deposited dust (DD)

Table 4 compares the contents of major and trace elements in the coal CPs sampled in our study with Chinese coals and worldwide

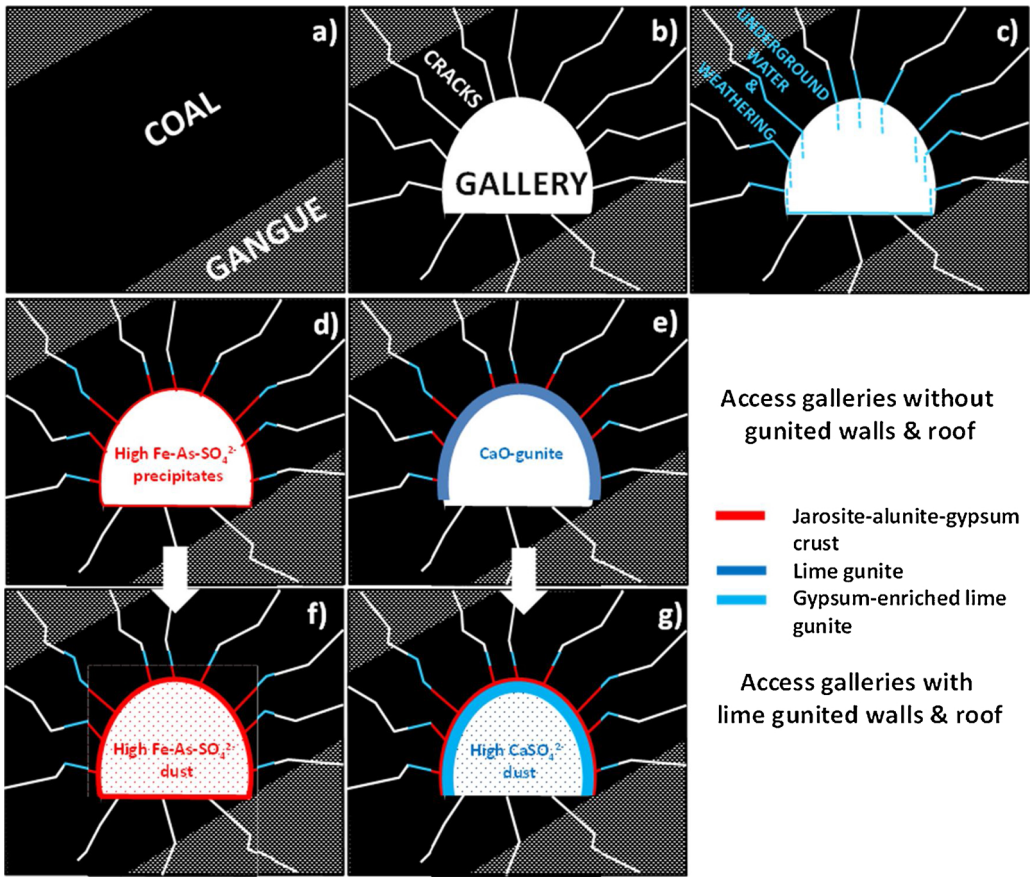

Fig. 3. Conceptual model for the emission of alunite-jarosite and gypsum dust in underground mines with and without gunited walls. a) to g) indicate the time sequence.

Table 4
Major and trace element contents in the coal seams worked (CP, average of channel profiles of the different seams) at the study underground mines and comparison with the respective China and Worldwide averaged concentrations (a. Dai et al., 2007, 2008; b. Ketris and Yudovich, 2009, respectively). Average coals of China and around the world, and all the coals channel profiles collected in the four undergrounds mines. BWC, Bituminous South-West China; SSC, Subbituminous South China; BSC, Bituminous South China; and ANC, Anthracite North China.

Element	CHINA[a]	WORLD[b]			BWC		SSC	BSC	ANC
		Brown	*Hard*	*All*	*CP #7*	*CP #11*	*CP D-3*	*CP #4 – 1*	*CP#2 – 1*
	%	%	%	%	%	%	%	%	%
Moisture	–	–	–	–	0.86	0.69	3.14	0.74	2.22
Ash yield	–	–	–	–	30.71	15.18	62.41	46.32	13.10
C	–	–	–	–	60.05	73.92	22.80	39.04	79.03
H	–	–	–	–	3.59	4.37	2.35	2.20	2.76
N	–	–	–	–	0.98	1.32	0.82	0.36	0.99
S	–	–	–	–	2.00	0.78	1.93	3.34	0.17
Ca	0.88	–	–	–	0.88	0.97	0.20	0.23	0.81
K	0.16	–	–	–	0.26	0.03	1.51	0.58	0.27
Fe	3.39	–	–	–	2.02	0.75	2.04	0.39	0.55
Mg	0.13	–	–	–	0.18	0.05	0.29	0.14	0.09
Na	0.12	–	–	–	0.05	0.03	0.24	0.12	0.23
Al	3.32	–	–	–	3.21	2.70	9.69	8.92	3.40
	mg/kg	mg/kg	mg/kg	mg/kg	mg/kg	mg/kg	mg/kg	mg/kg	mg/kg
Ti	1978	720 ± 40	890 ± 40	800	3900	1026	2627	2963	2972
Mn	116	100 ± 6	71 ± 5	86	201	19	80	16	78
P	402	200 ± 30	250 ± 10	230	72	503	380	708	501
Li	32	10 ± 1	14 ± 1	12	32	23	81	213	48
Be	2.1	1.2 ± 0.1	2.0 ± 0 .1	1.6	1.7	1.4	2.5	2.0	0.42
Sc	4.4	4.1 ± 0.2	3.7 ± 0.2	3.9	7.3	4.3	19	19	8.4
V	35	22 ± 2	28 ± 1	25	184	89	172	84	56
Cr	15	15 ± 1	17 ± 1	16	38	13	100	51	30
Co	7.1	4.2 ± 0.3	6.0 ± 0.2	5.1	11	11	13	3.9	22
Ni	14	9.0 ± 0.9	17 ± 1	13	28	16	44	17	23
Cu	18	15 ± 1	16 ± 1	16	85	35	51	25	22
Zn	41	18 ± 1	28 ± 2	23	27	35	74	23	44
Ga	6.6	5.5 ± 0.3	6.0 ± 0.2	5.8	12	8.5	27	27	13
Ge	2.8	2.0 ± 0.1	2.4 ± 0.2	2.2	3.8	2.2	3.2	2.3	1.5
As	3.8	7.6 ± 1.3	9.0 ± 0.7	8.3	3.4	4.3	12	6.5	3.0
Se	2.5	1.0 ± 0.15	1.6 ± 0.1	1.3	3.3	2.6	4.0	8.7	4.5
Rb	9.3	10 ± 0.9	18 ± 1	14	9.8	1.6	133	13	8.3
Sr	140	120 ± 10	100 ± 7	110	109	96	85	118	129
Y	18	8.6 ± 0.4	8.2 ± 0.5	8.4	19	19	24	46	16
Zr	90	35 ± 2	36 ± 3	36	82	45	121	231	145
Nb	9.4	3.3 ± 0.3	4.0 ± 0.4	3.7	15	7.4	9.6	16	15
Mo	3.1	2.2 ± 0.2	2.1 ± 0.1	2.2	0.25	0.27	9.5	9.0	11
Cd	0.25	0.24 ± 0.04	0.20 ± 0.04	0.22	< 0.1	< 0.1	0.15	0.32	< 0.1
Sn	2.1	0.79 ± 0.09	1.4 ± 0.1	1.1	2.9	2.2	3.4	4.2	2.8
Sb	0.84	0.84 ± 0.09	1.00 ± 0.09	0.92	< 0.1	0.41	3.0	0.51	0.23
Cs	1.1	0.98 ± 0.10	1.1 ± 0.12	1	0.61	< 0.1	14	4.5	0.39
Ba	159	150 ± 20	150 ± 10	150	112	84	300	27	107
La	23	10 ± 0.5	11 ± 1	11	26	21	29	52	24
Ce	47	22 ± 1	23 ± 1	23	52	41	57	106	51
Pr	6.4	3.5 ± 0.3	3.4 ± 0.2	3.5	6.3	4.9	7.8	12	6.0
Nd	22	11 ± 1	12 ± 1	12	23	18	25	41	24
Sm	4.1	1.9 ± 0.1	2.2 ± 0.1	2	5.1	4.1	6.0	9.5	6.0
Eu	0.84	0.50 ± 0.02	0.43 ± 0.02	0.47	0.68	< 0.1	1.0	1.4	0.61
Gd	4.7	2.6 ± 0.2	2.7 ± 0.2	2.7	3.9	3.2	4.0	7.0	3.8
Tb	0.62	0.32 ± 0.03	0.31 ± 0.02	0.32	0.29	< 0.1	0.31	1.1	0.43
Dy	3.7	2.0 ± 0.1	2.1 ± 0.1	2.1	4.1	3.4	4.7	9.3	3.7
Ho	0.96	0.50 ± 0.05	0.57 ± 0.04	0.54	0.32	0.52	0.89	2.0	0.50
Er	1.8	0.85 ± 0.08	1.0 ± 0.1	0.93	1.9	1.9	2.7	4.9	1.0
Tm	0.64	0.31 ± 0.02	0.30 ± 0.02	0.31	< 0.1	< 0.1	0.22	1.2	0.27
Yb	2.1	1.0 ± 0.1	1.0 ± 0.06	1	1.9	2.0	2.6	5.1	1.3
Lu	0.38	0.19 ± 0.02	0.20 ± 0.01	0.2	< 0.1	< 0.1	< 0.1	0.45	0.17
Hf	3.7	1.2 ± 0.1	1.2 ± 0.1	1.2	4.0	2.5	4.2	7.4	4.3
Ta	0.62	0.26 ± 0.03	0.30 ± 0.02	0.28	0.41	0.26	0.20	0.22	0.52
W	1.1	1.2 ± 0.2	0.99 ± 0.11	1.1	0.36	< 0.1	1.3	2.3	0.89
Tl	0.47	0.68 ± 0.07	0.58 ± 0.04	0.63	< 0.1	< 0.1	1.0	< 0.1	< 0.1
Pb	15	6.6 ± 0.4	9.0 ± 0.7	7.8	13	11	31	38	31
Bi	0.79	0.84 ± 0.09	1.1 ± 0.1	0.97	< 0.1	< 0.1	0.29	0.82	0.38
Th	5.8	3.3 ± 0.2	3.2 ± 0.1	3.3	6.9	6.0	15	22	17
U	2.4	2.9 ± 0.3	1.9 ± 0.1	2.4	2.5	1.7	7	10	3.3

averages (Dai et al., 2008, 2007; Ketris and Yudovich, 2009). Although most of the major and trace elements in the coals sampled fall within the usual range described for Chinese coals, several relevant differences are reported below:

i) BWC mine: Concentration coefficient (CC, the ratio of the concentration in the coal divided by the reference concentration) of V reaches 2.5, and those of Mo, W, Cs, Bi, Mn, Rb, K, Tl Fe, Na, Mg, Cd and Ta vary across a range from 0.1 to 0.4. Furthermore, in coal #7,

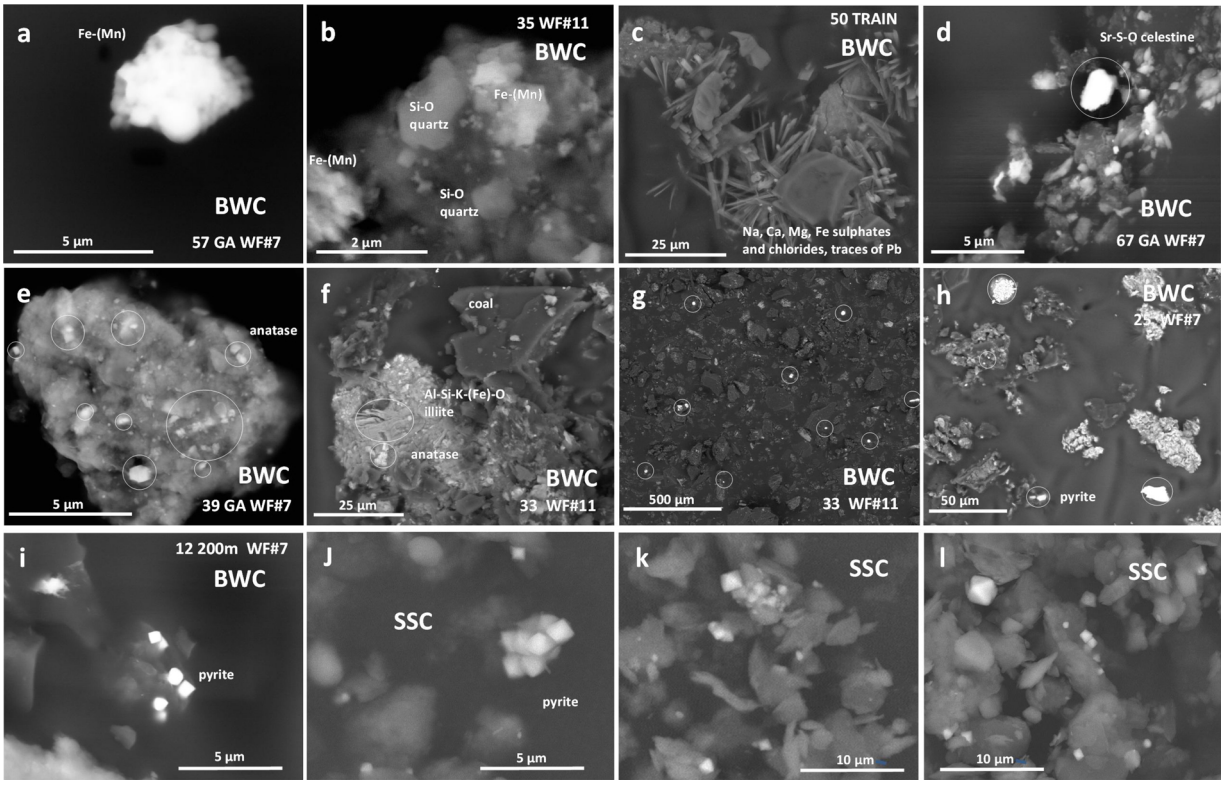

Fig. 4. Scanning electron microscopy (SEM) images showing diverse aspects redacted in all of this study. (a–b) shows the occurrence of metallic Fe-Mn particles in the suspended dust sampled at WF #7 and #11, c-d) shows the occurrence of Ca-Na sulphates and celestine in suspended dust from BWC, (e–f) shows the occurrence of anatase in very fine crystal aggregates, (g–i) shows the occurrence of pyrite in suspended dust from the BWC mine present as isolated particles, and (j–l) shows the occurrence of isolated pyrite crystals in the RDD from the SSC D3 and BWC #7 coals. In the first case the framboidal pyrite aggregates are embedded into a kaolinite matrix while in the second these are into the maceral matrix.

the CCs of Ti, Ni, Cr, Cu and V reach from 2.0–5.3 and from 0.1 to 0.4 for Mo, Sb, Bi, P, Tl, W, Cd and Na.

ii) SSC mine: Subbituminous coal highly enriched in Na, Pb, Mg, Tl, Li, Th, Cu, U, Al, Mo, As, Ni, Sb, Ga, Sc, V, Cr, K, Cs, and Rb with CCs from 2.0–14.3, and depleted in only Ca, Ta and Bi (0.2 − 0.4).

iii) ANC mine: Anthracite highly enriched in Pb, Th, Co and Mo (CCs = 2.0–3.6) and depleted in Fe, Be, Tl, Sb, Cs and Cd (0.2 − 0.4) when compared with the Chinese coal averages.

iv) BSC mine: Bituminous coal highly enriched in a large number of elements. Thus, CC values reach 2.0–6.6 for Sn, Hf, W, REE's, V, Pb, Zr, Y, Al, Mo, Cr, Se, K, Th, Cs, Ga, U, Sc and Li, and 0.1 − 0.4 for Fe, Mn, Ba, Tl, Ca and Ta.

The DD samples from the ANC, BWC, BSC and SSC mines are geochemically similar to the parent coals described above. Relevant differences are discussed below (Tables S4 and S5).

BWC mine:

i) Relative to the DD from WF #11, the WF #7 DD is enriched in most major and trace elements associated with aluminium-silicate and sulphide and phosphate minerals due to its higher ash yields. Dust from #11 is only enriched vs #7 in Zn, which is usually associated with sulphide in coal.

ii) With respect to the CP (DD/CP = 7.0), WF #7 DD is highly enriched in P, which could be associated with the higher phosphate mineral content in the DD. Furthermore, it is also enriched in Ca, Fe, Ti, Cr, Co, As, Cs, Zn, Sr, Mg, Mn, Ta, Ba K, Na Rb and Ni (DD/CP = 1.5–3.0). The same applies for Mn in #11 (DD/CP = 5.1) as well as Mg, V, Cr, K, Rb, Ti and Zn (1.5–2.5).

iii) The DD in the access galleries is highly enriched in Fe, As, Sb and S compared to samples from the WFs, in parallel with the jarosite-alunite enrichment.

iv) The galleries with lime gunited walls are highly enriched in Ca, Zn and S. In line with the foregoing discussion, the AMD reaching the lime gunited walls can be considered to be the source of the water with high sulphate content that generates gypsum when interacting with lime. This gypsum can be emitted from the walls and deposited with the dust.

v) The DD on the floor of the wagons (worker transport) is enriched in Ca, Fe, Mn, Cr, Zn, As, Sr, Sb and Pb with respect to the DD samples from WFs #7 and #11, maybe related to wear from mining machinery in the WF, which could emit metals such as Mn, V, Cr, Fe, Ni, Co and Zn.

vi) Lastly, the DD from the coal mill has similar major and trace element content to that of the CPs, with slightly higher concentrations of Zn, As and Pb. In contrast, the Mn concentration in the coal mill is lower than that in the DD collected in the WFs.

SSC mine:

i) The DD from the WF is highly enriched (compared to the CP) in Sb (DD/CP = 16), and, to a lesser extent, in Mn and Zn (5.0), and also in Ge, Co, Fe, Bi, Ca, As, Cu, Cd and Ta (1.5–3.7).

ii) The DD from the access gallery has similar or slightly lower concentrations of most elements (Tables S4 and S5), except for Fe, Mn, As, Sn, Sb and Pb, and especially Zn. Concentrations of Zn in the DD increase as a function of the distance from the WF, e.g. 25 m out (524 mg/kg), 50 m out (2734 mg/kg) and 100 m out (4893 mg/kg), when starting at 385 mg/kg in the DD in the WF.

iii) The DD sample of a gallery with a coal and gangue belt is characterised by a much lower Mn content and higher Na, Pb, and especially As (x2) than the corresponding contents in the WF.

iv) Lastly, the coal mill DD is characterised by slightly low contents of most elements but higher P and S (Tables S4 and S5).

BSC mine:

i) In this inactive mine, elements with a high DD/CP rate include Ca and As (10 and 13), Zn (50) and Sb (175) but also Cu, V, U, Co, Mg, Cr, Ba, Mo, Cd, Sr, Ta, Mn, W and Fe (1.5–5.5).
ii) Concentrations of most major and trace elements in the DD samples from the access gallery and the WF are very similar, with the exception of Ca and Sr (probably from the lime gunited walls, higher in the 50 m than the 100 m DD samples; Zn (x10)), As and Sb (much higher in the 100 m dust sample than in the 50 m one).

ANC mine

i) The chemical composition of the DD sample from the return air shaft, compared with that of the CP showed a DD enrichment in Ca, As (9) and Sb (53) but also in Ba, Zn, Ta, S, Sr, Na, W, Pb, Be, Fe, K, Mg, Rb, Cs and Mg (DD/CP from 1.5 to 5).

In terms of a general pattern for most mines, it is worth noting that the DD/coal enrichment of a number of elements is potentially associated with the wear on mining machinery (Fe, Mn, V, W, Cr, Ni, Co, depending on the mine). Fig. 4 shows the occurrence of different minerals under the scanning electron microscope including metallic Fe-Mn particles in the DD sampled at WFs #7 and #11 (Fig. 4a and b). Elements associated with salts (such as gypsum, jarosite and alunite) from AMD (Fe, As, Sb, Zn, Pb, Mn, Mg, and Na, also depending on the mine) also have high DD/coal enrichment. The latter suggests the emission of jarosite-alunite, usually enriched in As, Sb, Pb, Cd, Zn and Ba, among others, either from the walls of the galleries or from process (i) described in the prior section. In any case, As and Sb arise from AMD; therefore, guniting the walls of the galleries might therefore reduce As and Sb content in the dust from these areas. On the other hand, the significant of Zn, especially in the access galleries of the BSC and SSC mines, might be ascribed to wear emissions from the metallic cylinders of the mine belts.

The DD sample taken on the floor of the train in the BWC mine is enriched in a large number of elements compared to the DD samples from WFs #7 and #11, which is probably due to the contributions of the gunited lime walls (Ca and Sr), rails and brakes (Fe, Mn, Cr, Zn, Sb and Pb (Font et al., 2019; Moreno et al., 2015) and jarosite dust (Fe, Sb, As, Pb).

3.4. Mineralogy and composition of the respirable fraction of deposited dust (RDD)

Table 5 shows the 25th (D25), 50th (D50), 75th (D75), and 90th (D90) percentiles of the size distributions of the RDD samples. All RDD samples have D50 s in the range of 3 − 5 μm, with most concentrating around 4 μm, confirming that we succeeded in separating the respirable fraction from the DD samples. On the other hand, the D90 values are in the 6 − 10 μm size range, which indicates that RDD samples separated by the PM10 and PM2.5 device have grain sizes < 10 μm.

Fig. 5 (top) shows the RDD/DD ratios for the mineral content in the samples. The results demonstrate a depletion of quartz (RDD/DD = 0.6 ± 0.2) and carbonate minerals (0.6 ± 0.3) as well as lower proportions of feldspars (0.8 ± 0.4), sulphides (0.8 ± 0.5) and sulphates (0.8 ± 0.5) in the RDD (< 4 μm) but very similar contents of anatase (1.0 ± 0.7) and clay minerals (1.1 ± 0.1) compared with the DD (< 500 μm). Accordingly, the results show that, on average, the mineralogy of the RDD is similar to that of the DD, with a constantly higher content of quartz (RCS) and carbonate minerals. However, the variability among samples might be high (e.g. 68% relative standard deviations for quartz and anatase).

Table 5
Percentile 25, 50, 75 and 90 (D25, D50, D75 and D90, in μm) of the grain size distribution of the respirable deposited dust (RDD). WF, Working front; GW, Gunited walls; FTW, Floor of train wagons.

Mine	Location	D25	D50	D75	D90
Bituminous South-West	GW #7	3.37	4.93	6.99	9.74
Bituminous South-West	300 m WF #7	3.25	4.40	7.58	9.66
Bituminous South-West	100 m WF #7	3.39	4.45	7.37	9.20
Bituminous South-West	50 m WF #7	3.25	4.68	6.58	9.11
Bituminous South-West	WF #7	2.91	4.25	5.97	8.23
Bituminous South-West	WF #11	3.06	4.42	6.16	8.42
Bituminous South-West	FTW	2.49	3.85	5.47	7.57
Subbituminous South	2000 m WF D-3	2.48	3.99	5.87	8.37
Subbituminous South	100 m WF D-3	2.38	3.70	5.27	7.30
Subbituminous South	WF D-3	1.64	3.14	4.41	5.92
Subbituminous South	Coal mill	2.45	3.87	5.61	7.91
Bituminous South	100 m WF #4 − 1	2.77	4.24	6.26	9.17
Bituminous South	50 m WF #4 − 1	2.50	3.90	5.64	7.94
Anthracite North	Air shaft #2 − 1	2.63	4.61	7.75	10.11
Anthracite North	Air shaft #2 − 1	2.39	4.20	7.89	9.32

Same ratio but for each mine is shown in Fig. 5 (bottom). Low RDD/DD ratios in 3 mines (bituminous coal and anthracite, usually < 1 and, in most cases, < 0.75) reveal a general depletion of most minerals in hard coals, with the exception of anatase (1.4) in the BSC mine and clay minerals (1.4, and especially 1.8 kaolinite-clinochlore) in the ANC mine. However, for the subbituminous coal (SSC mine), there are a number of minerals with significant RDD/DD enrichment such as the sulphate and sulphide minerals and feldspars (1.2 − 1.7). It is interesting to note a constantly low RDD/DD for quartz in all mines.

Thus, it seems that quartz (RCS) and carbonate minerals are depleted in most RDD samples when compared with the DD samples. For the other minerals, a high variability was found, most likely due to differences in the size occurrence modes of the minerals in the parent coal and the mining operation patterns. It is also evident that hard coals are more depleted in RDD/DD for most minerals compared with the soft coal studied.

Table 6 shows that the RCS content is markedly higher in the SSC RDD samples (from a coal with very high ash yield), with concentrations ranging from 9.6–19.7% in the RDD, while, in most RDD samples from the BWC, BSC and ANC mines, the RCS content reaches up to 1.4–7.5%, with one BWC sample at < 0.1%. When we refer these RCS contents to the basis of the DD (i.e. deposited dust < 500 μm), these concentrations reach 1.8–6.5% for SSC and 0.1 to 0.8% for all the other samples, with the exception of 2.2% in a BSC sample and < 0.1% in one BWC sample.

Fig. 6 (top) shows the RDD/DD ratios for the major elements, with ratios from 0.6 to 0.8 for Fe (0.6 ± 0.3), Ca (0.8 ± 0.3) and Mg (0.8 ± 0.3) (usually with Fe-sulphide and/or carbonate affinity in our samples) and from 0.9 to 1.1 for the other major elements (with sulphide, sulphate, aluminium-silicate, anatase or phosphate affinities). Thus, indicating once again a decrease in carbonate-associated elements in the RDD compared to the DD and a similar content in the case of the aluminium-silicate fractions. In spite of this general trend, Fig. 6 (bottom) shows, as described above for most minerals, that for hard coals, the RDD/DD values are < 1 for most elements and samples, while, for the soft coal, there is an opposite trend.

For trace elements (Fig. 7, top), Mo, Mn, Be, and Nb have average RDD/DDs from 0.7 to 0.8, whereas W, Se, Cs, Cd, Sb and As reach values from 1.2 to 1.4, with all other elements showing very similar contents in RDD and DD. Again these averaged patterns might be quite different from those from the individual mines (Fig. 7 bottom), depending on the mode of occurrence of these trace elements, the size of the minerals containing them in the parent coal seams, and the specific operating patterns of the mine.

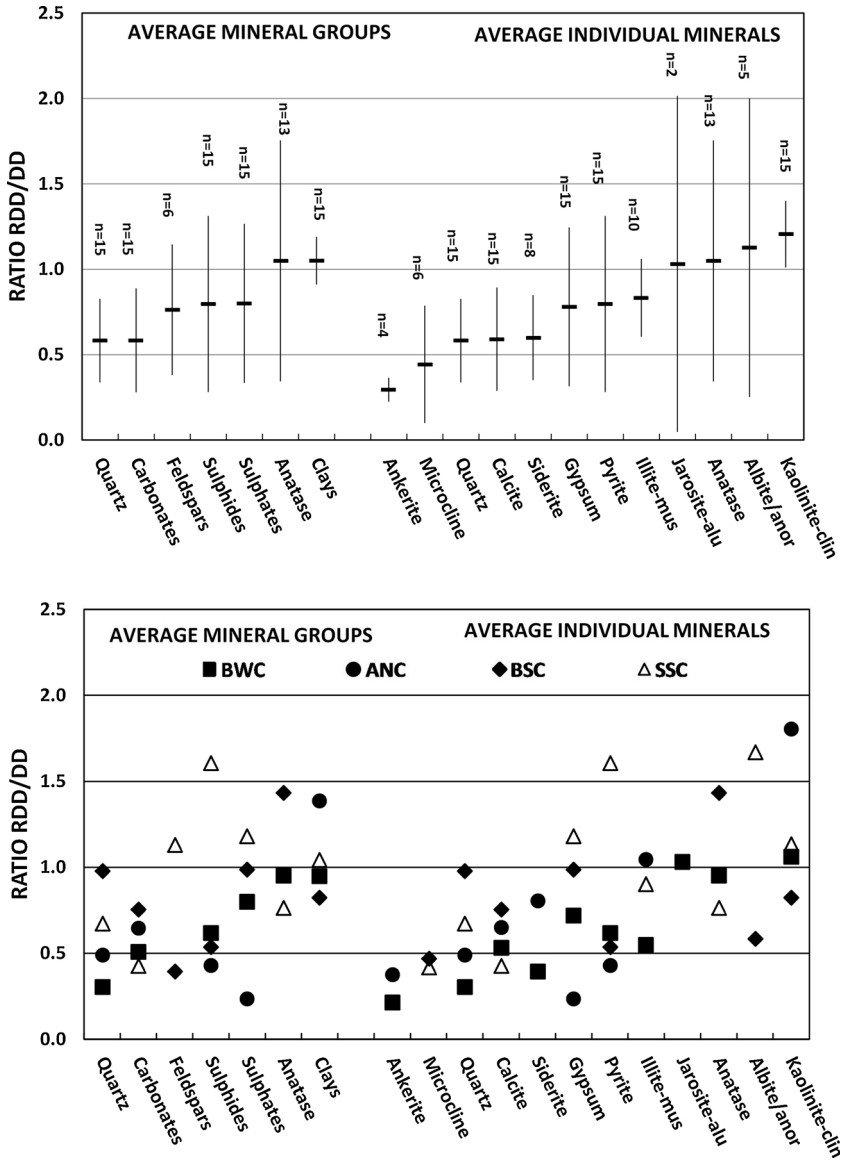

Fig. 5. Ratio of mineral contents determined by XRD analysis in the respirable deposited dust (RDD) and the parent deposited dust (DD < 500 μm) (RDD/DD). Top: Average ratios ± SDV for the 4 mines; bottom: average for each mine.

Table 6
Content of respirable crystalline silica (RCS,%) in the respirable deposited dust (RDD) and re-calculated content with the basis of RCS content in the respective deposited dust finer than 500 μm (DD). WF, Working front; GW, Gunited walls; FTW, Floor of train wagons.

Mine	Location	RCS in RDD	RCS in DD
Bituminous South-West	GW #7	1.4	0.2
Bituminous South-West	300 m WF #7	4.6	0.8
Bituminous South-West	100 m WF #7	4.7	0.2
Bituminous South-West	50 m WF #7	4.6	0.6
Bituminous South-West	WF #7	4.0	0.6
Bituminous South-West	WF #11	< 0.1	< 0.1
Bituminous South-West	FTW	3.3	0.3
Subbituminous South	2000 m WF D-3	9.6	3.6
Subbituminous South	100 m WF D-3	16.9	6.5
Subbituminous South	WF D-3	19.7	4.2
Subbituminous South	Coal mill	14.6	1.8
Bituminous South	100 m WF #4 − 1	7.5	2.2
Bituminous South	50 m WF #4 − 1	3.2	0.8
Anthracite North	Air shaft #2 − 1	3.2	0.8

3.5. CIP-10T analysis

Two CIP-10T samples were taken in the BWC mine, one on the way to WF #7 (from the railway station to the WF, 1 h in the WF and back, with a total duration of the sampling of 5.3 h), and the second one on the way to WF #11 (similar to path taken in WF #7 but with a duration of 3.6 h). The PM10 averaged levels during this time period (5.3 and 3.6 h, of which 1.5 h was spent in the respective WF) reached 3204 and 4,578 μg/m^3 for WF #7 and WF #11, respectively, and PM10 − 200 levels of 5,442 and 14,618 μg/m^3 were sampled, respectively, which is equivalent to a total suspended particle (TSP) concentrations of 8646 and 16,671 μg/m^3, respectively. The higher average levels for the WF #11 sample are probably due to the higher relative weight of the 1.5 h sampling in the WF (1.5/3.6 h) on the bulk sampling compared to the one from WF #7 (1.5/5.3 h). In fact, TSP concentrations measured at 5 min intervals with an optical device by the security staff of the BWC mine reached 14,000–76,000 μg/m^3 in WF #11 and 8100 − 57,700 μg/m^3 in WF #7.

Table 7 shows the occupational levels of major and trace elements in the PM10 and PM10 − 200 measured in the BWC mine when travelling in and out and working at WFs #7 and #11. As would be expected

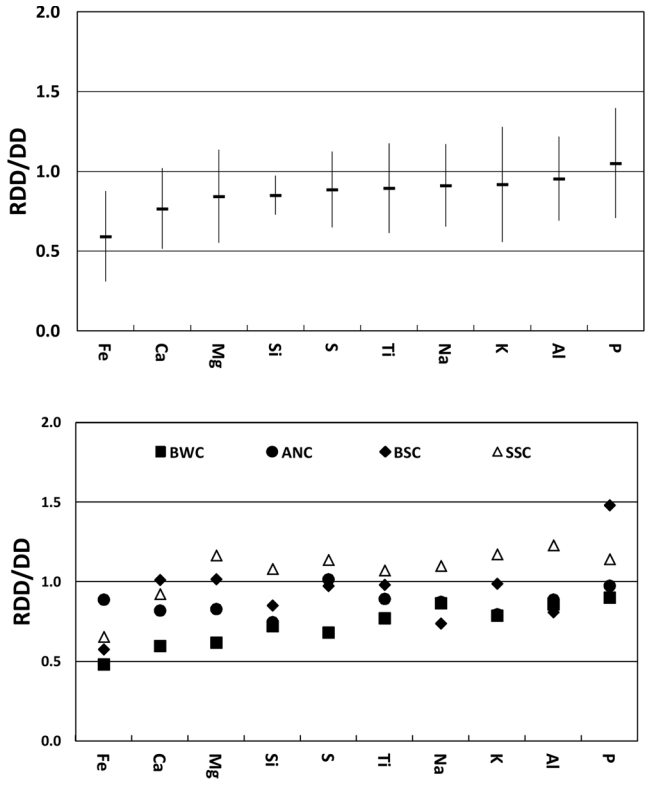

Fig. 6. Ratio of major element contents in the respirable deposited dust (RDD) and the parent deposited dust (DD < 500 µm) (RDD/DD). Top: Average ratios ± SDV for the 4 mines; bottom: average for each mine.

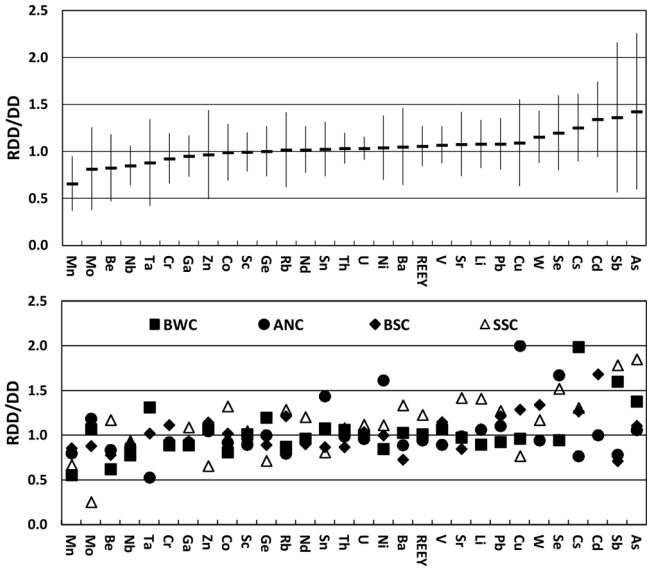

Fig. 7. Ratio of trace element contents in the respirable deposited dust (RDD) and the parent deposited dust (DD < 500 µm) (RDD/DD). Top: Average ratios ± SDV for the 4 mines; bottom: average for each mine.

from the high dust concentrations, the levels are very high, and the sum of all the components reaches around 15–17% of the PM10 and PM10 − 200 levels, which is close to the 11 − 23% ash yields obtained for the DD samples. We evaluated the major and trace elements in the occupational PM10 (sampled using the CIP-PM10 samplers) with those in two composite RDD chemical profiles created from the access and WF gallery results and modulated by the relative time spent in each of them (Table S3). It should be noted that the RDD is equivalent to PM4

Table 7
Levels of major and trace elements in PM10 and PM10-200 occupational exposure samples collected in the Bituminous South-West China (BWC) underground mine.

	PM10 #7	PM10 − 200 #7	PM10 #11	PM10 − 200 #11
	(µg/m^3)	(µg/m^3)	(µg/m^3)	(µg/m^3)
PM10 − 200	–	7973	–	9977
PM10	3204	–	4578	–
CO_3^{2-}	87	142	92	186
SIO_2	212	529	258	803
Al_2O_3	104	203	134	336
Fe	15	123	68	60
S	34	66	43	109
Ca	35	57	37	75
MgO	3.3	41	15	9.3
MnO	0.26	3.3	1.4	0.78
TiO_2	7.5	42	23	22
K_2O	8.0	17	10	28
Na_2O	5.2	10	6.7	17
P_2O_5	1.6	3.2	2.1	5.3
	(ng/m^3)	(ng/m^3)	(ng/m^3)	(ng/m^3)
Li	92	61	72	154
Sc	19	47	23	53
V	261	600	501	1163
Cr	49	980	134	2487
Co	36	102	42	106
Ni	47	533	106	1453
Cu	288	525	210	1007
Ga	31	63	34	78
Rb	15	132	46	22
Sr	471	919	521	928
Y	66	74	54	167
Zr	226	727	352	854
Ba	204	717	405	391
As	153	369	684	181
La	88	166	93	245
Ce	166	355	200	455
Nb	18	88	37	63
Pr	20	40	22	52
Nd	69	144	80	183
Sm	16	28	17	39
Gd	12	19	< 0.1	28
Dy	13	18	< 0.1	33

and not PM10, but it was not possible to sample PM4 with the CIP instrumentation. In the case of the WF #11 trip, the CIP-PM10/RDD ratios for most major (0.9–1.4) and trace (0.7–1.4) elements is small, with the exception of Ca (0.4) and As (2.6). In the case of WF #7, the CIP-PM10 concentrations of major and trace elements are in many cases lower than those found in the RDD, with CIP-PM10/RDD ratios from 0.3 to 0.5 for most major elements, with the exception of Al (0.8), and between 0.7 and 1.4 for most trace elements, except for As (2.6) and Ti, V, Cr, Mn, Ni, Rb, Nb and Ba (0.3 − 0.6). Accordingly, our results reveal that the composition of the occupational PM10 is quite close to the RDD composition indicated by the CIP-PM10 for WF #11, but is reduced by around 50% for most major and trace elements in the case of the CIP-PM10 for WF #7. We do not have an obvious explanation for this difference because we followed the same protocol in both cases, with the main difference being that during sampling with the CIP-PM10, WF #11 remained active at all times, but WF #7 remained active during only one third of the sampling time.

China's Occupational Exposure Limit (OEL) for time-weighted average exposure value (TWA) for over 8 h of As is fixed at 10 µg/m^3 (Liang et al., 2006), whereas in the BWC mine, 0.1 and 0.7 µg/m^3 were reached. Moreover, also in China, for coal dust with < 10% crystalline silica, the TWA OELs for TSP and respirable fractions (PM4) are fixed at 4,000 and 2,500 µg/m^3, respectively, while, for coal dust with 10–50% crystalline silica, these values are fixed at 1000 and 700 µg/m^3, respectively (Liang et al., 2006). In this study the occupational exposure concentrations reached 11,177 and 15,555 µg/m^3 for TSP and 3204 and 4,578 µg/m^3 for the inhalable fraction (PM10) for WF #7 and WF #11,

Table 8
Oxidation potential (OP) for Ascorbic Acid (AA), glutathione (GSH) and total (TOT) obtained for the samples of respirable deposited dust (RDD) from the different underground coal mines. WF, Working front; GW, Gunited walls; FTW, Floor of train wagons.

Mine	Location	OP^{AA}%/μg	± SD	OP^{GSH}%/μg	± SD	OP^{TOT}%/μg
Bituminous South-West	GW #7	0.7	0.05	0.5	0.00	1.2
Bituminous South-West	300 m WF #7	1.2	0.01	< 0.1	–	1.1
Bituminous South-West	100 m WF #7	2.0	0.00	0.2	0.06	2.2
Bituminous South-West	50 m WF #7	0.9	0.08	< 0.1	–	0.9
Bituminous South-West	WF #7	0.8	0.06	0.1	0.02	0.9
Bituminous South-West	WF #11	0.1	0.04	0.0	0.05	0.1
Bituminous South-West	FTW	0.2	0.00	0.0	0.01	0.2
Subbituminous South	2000 m WF D-3	0.6	0.04	0.0	0.03	0.6
Subbituminous South	100 m WF D-3	0.5	0.02	0.1	0.02	0.6
Subbituminous South	WF D-3	0.5	0.01	0.2	0.07	0.6
Subbituminous South	Coal mill	0.4	0.03	0.1	0.07	0.5
Bituminous South	100 m WF #4 – 1	0.5	0.04	0.1	0.07	0.6
Bituminous South	50 m WF #4 – 1	0.7	0.03	0.1	0.08	0.7

respectively, but at 5.3 – 3.6 h, respectively, as opposed to the 8 h required for the TWA.

3.6. Toxicology: oxidative potential (OP)

As far as we know our study presents the first data on OP^{AA} and OP^{GSH} of coal mine dust. The analysed samples display a negligible amount of oxidation towards urate. Past experience with a variety of PM samples has shown that urate is not usually susceptible to oxidisation by PM (Soltani et al., 2018), and, in fact, it is used as a control for the experiment. AA and GSH are both important antioxidants with low molecular weight found within the respiratory tract lining fluid (RTLF) (Kelly, 2003). Their depletion by PM indicates that they play a protective role against PM when it enters the airways, as they have a suicidal reaction, i.e. they react with oxidants present (or generated) on the PM to decrease the OP of the PM, thus reducing its ability to cause harmful oxidative reactions when it reaches the lung surface. As shown in Table 8, the five RDD samples from the BWC mine's WF #7, especially the one collected 50 m away from the WF, stand out from the rest with regards to oxidant activity towards OP^{AA}. These samples were collected in the same area nearby WF #7, but no trend between OP^{AA} and the distance to this WF is observed. The sample collected at the BWC mine in the lime gunited gallery close to WF #7 is again the most active against GSH (OP^{GSH}), followed by the BWC sample 50 m away from this WF, and a SSC mine sample from the WF. Thus, in the same BWC mine, the RDD from WFs #7 and #11 yield very different values for OP^{AA}, with the highest OP^{AA} concentration in the RDD sample with higher ash yields and metal content.

The NIST1648a control yielded 35% of AA consumption, compared to 35–100% for all BWC WF #7 samples, < 10% for all BWC WF #11 samples, and 20–30% for samples from the SSC and BSC mines. In terms of GSH consumption, the NIST control reached 15% OP^{GSH}, while 25% was attained by the lime gunited gallery RDD from WF #7 in the BWC mine, and < 10% was obtained by all the other samples.

Fig. 8 compares the normalised OP^{TOT} ($OP^{AA} + OP^{GSH}$, in %consumption/μg) of the RDD samples from our study with both the NIST control, and equivalent results from the Chamonix Valley in summer and winter (the latter with high PM contributions from biomass burning) (Calas et al., 2018) as well as subway PM from six stations in Barcelona (Moreno et al., 2017) and PMs from indoor and outdoor locations around a Fe-ore facility in Iran (Soltani et al., 2018). As shown in this figure, the average RDD OP^{TOT} for the three coal mines is 6.9-fold lower than Chamonix-winter PM (probably due to the high content of PAHs from biomass burning) and 1.6–2.3-fold lower than the NIST urban, Fe-ore, Chamonix-summer and Barcelona subway PM. However, values obtained for the WF #7 RDD are relatively higher and similar to those found for the NIST urban, Fe-ore and Chamonix-summer PM and 1.9–3.3 fold lower than those found for the Barcelona subway and

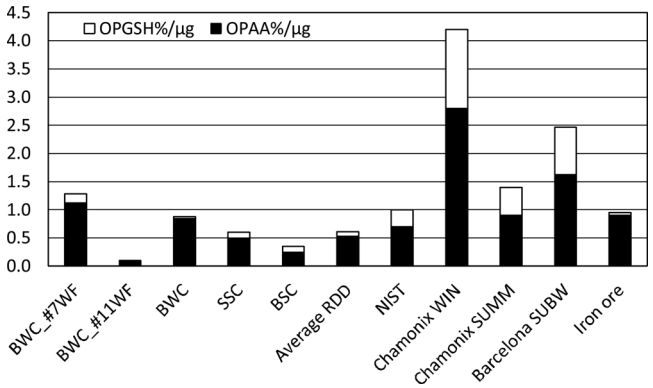

Fig. 8. Normalised total oxidative potential ($OP^{TOT} = OP^{AA} + OP^{GSH}$, in %consumption/μg) of the respirable deposited dust (RDD) samples from our study with the NIST urban particles, and results from the Chamonix Valley in summer and winter (the latter with high biomass burning PM contributions) (Calas et al., 2018); subway PM from six stations in Barcelona (Moreno et al., 2017), and PM from indoor and outdoor around Fe-ore facility in Iran (Soltani et al., 2018).

Chamonix-winter PM. Another contrasting piece of evidence is the < 0.1 rate obtained for OP^{GSH}/OP^{AA} for the RDD from the coal mines and Fe-ore PM, while, for the urban, subway and Chamonix Valley PM, this ratio reaches 0.4 – 0.6, most likely due to the higher relative influence of Fe on the OP of the samples in the RDD and Fe-ore PM, with more influence on the OP^{AA} than the OP^{GSH} (see below). The mode of occurrence of Fe and probably its oxidation state, however, must play a key role since the subway study found extremely high Fe levels but relatively low OP.

A cross correlation analysis of the OP^{AA} and OP^{GSH} of the RDD samples with their respective content of major and trace elements and mineral contents, as well as the particle size distribution, was carried out to identify major drivers of the OP. Most RDD components did not show correlation with OP values, but a reduced number of them accounted for a high proportion of the OP variance.

For RDD samples from BWC mine, excluding the one from the wagon's floor, OP^{AA} was markedly and positively correlated ($p < 0.05$) with the contents of Mo ($R^2 = 0.67$), S (0.78) and Fe (0.98); and with quartz (0.60), sulphates (0.70), pyrite (0.82), and anatase (0.94). Furthermore, OP^{GSH} values correlated positively with the contents of Mg, K, Cr, Pb ($R^2 = 0.74 - 0.79$), calcite, Zn, Rb, Sb, As, Cs, Ba, Ca, Na (0.81 – 0.88) and Sr (0.95).

When RDD from the two bituminous coal mines (BWC and BSC, excluding again the one of wagon from BWC) were considered, OP^{AA} was highly and positively correlated ($p < 0.05$) with Fe ($R^2 = 0.97$), and also with sulphate minerals (0.62), pyrite (0.71) and anatase

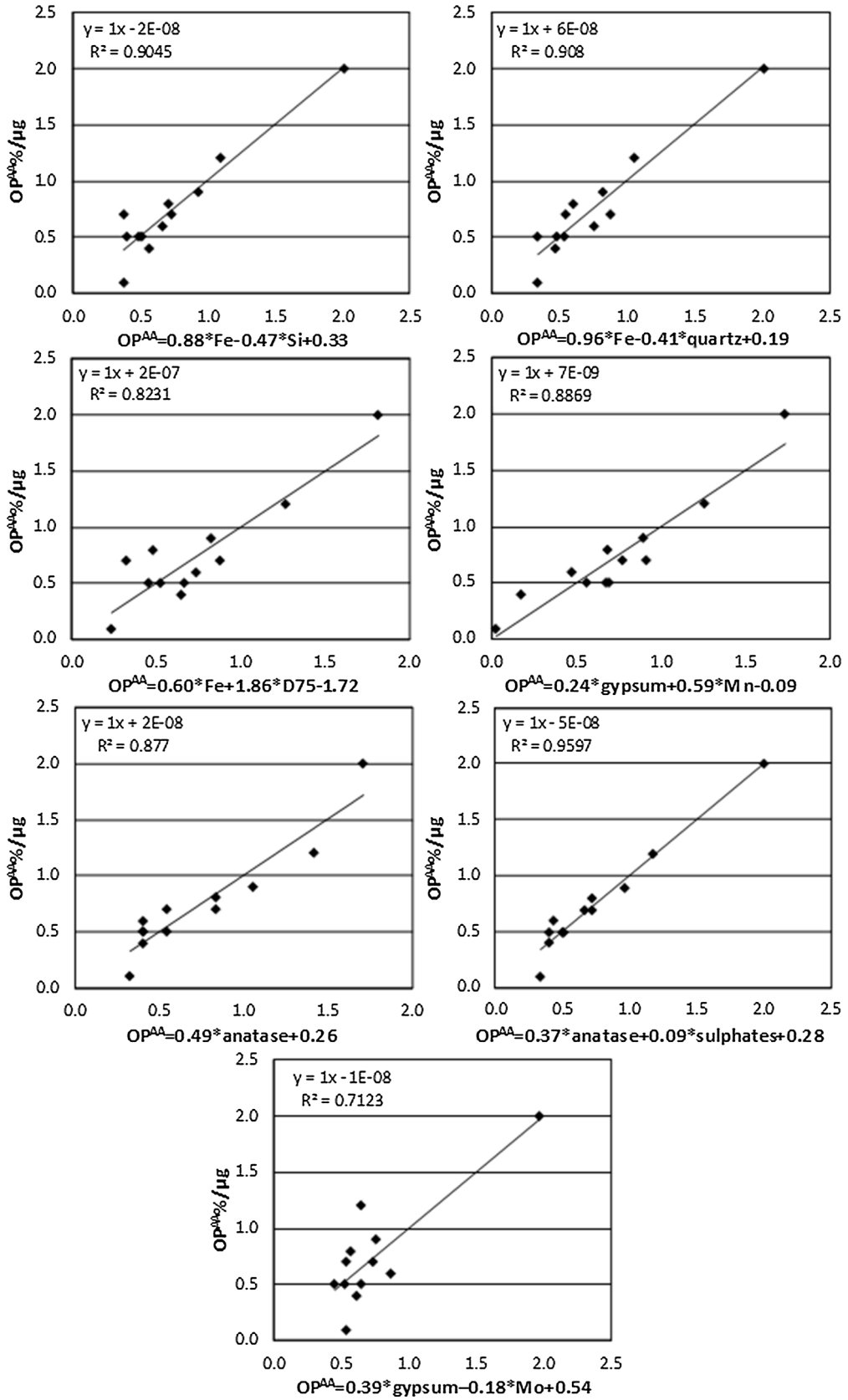

Fig. 9. Cross correlation plots of total Ascorbic Acid (OP^{AA}) in %consumption of antioxidant/µg of the respirable deposited dust (RDD) and the normalised content of specific elements and minerals. All RDD samples from all mines included, with the exception of the one from the floor of the train wagons of BWC.

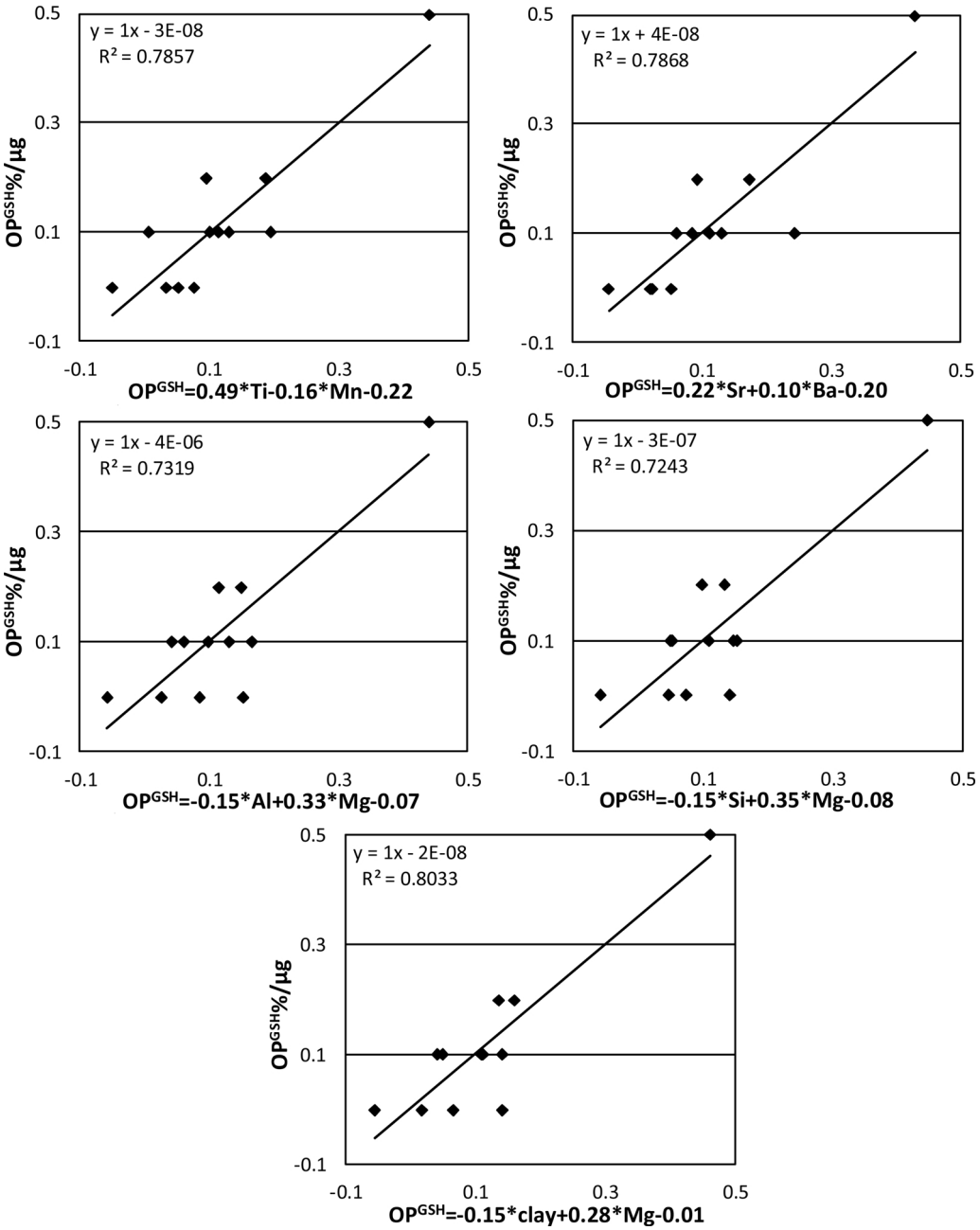

Fig. 10. Cross correlation plots of (top) the total glutathione (OP^{GSH} in %consumption of antioxidant/µg of the respirable deposited dust, RDD) and the normalised content of specific elements. All RDD samples from BWC and BSC mines included, with the exception of the one from the floor of the train wagons of BWC.

(0.89); and OP^{GSH} with Ba, Mg, Sr (0.64 − 0.69), calcite, Ca and Na (0.80 − 0.85).

In the case of the RDD from the subbituminous coal mine (SSC), OP^{AA} values correlated ($p < 0.05$) only with contents of Ca ($R^2 = 0.94$); and the OP^{GSH} ones with those of Cu, quartz, Cs and Ba (0.87 − 0.99).

A light positive correlation ($R^2 = 0.45$, $p = 0.07$) between particle size (D75) and OP^{AA} for the RDD of the two bituminous coal mines was found, and no correlation for the subbituminous coal RDD.

A multilinear regression analysis was carried out to identify the major RDD components governing the OP^{AA} (Fig. 9) and OP^{GSH} (Fig. 10) variability of RDD. Again all samples were included in the analysis with the exception of the one from the wagon of the BWC mine. To this end the concentration of each element and mineral was normalised with respect to the average concentrations of the 12 RRD samples. The main multivariate relationships found with a high statistical significance ($p < 0.05$) for slopes and constants of the regression equations were:

$$OP^{AA} = 0.88*Fe - 0.47*Si + 0.33 \ (R^2 = 0.91) \quad (10)$$

$$OP^{AA} = 0.96*Fe - 0.41*quartz + 0.19 \ (R^2 = 0.91) \quad (11)$$

$$OP^{AA} = 0.60*Fe + 1.86*D75 - 1.72 \ (R^2 = 0.82) \quad (12)$$

$$OP^{AA} = 0.24*gypsum + 0.59*Mn - 0.09 \ (R^2 = 0.89) \quad (13)$$

$$OP^{AA} = 0.49*anatase + 0.26 \ (R^2 = 0.88) \quad (14)$$

$$OP^{AA} = 0.37*anatase + 0.09*sulphate\ minerals + 0.28 \ (R^2 = 0.96) \quad (15)$$

$$OP^{AA} = 0.39*gypsum - 0.18*Mo + 0.54 \ (R^2 = 0.96) \quad (16)$$

$$OP^{GSH} = 0.49*Ti - 0.16*Mn - 0.22 \ (R^2 = 0.79) \quad (17)$$

$$OP^{GSH} = 0.22*Sr + 0.10*Ba - 0.20 \ (R^2 = 0.79) \quad (18)$$

$$OP^{GSH} = -0.15*Al + 0.33*Mg - 0.07 \ (R^2 = 0.73) \quad (19)$$

$$OP^{GSH} = -0.15*Si + 0.35*Mg - 0.08 \ (R^2 = 0.72) \quad (20)$$

$$OP^{GSH} = -0.15*clay + 0.28*Mg - 0.01 \ (R^2 = 0.80) \quad (21)$$

Where the OP^{AA} or OP^{GSH} values are given in % consumption AA or GSH/μg; and the elements and minerals, the normalised concentration versus the respective average contents of the 12 RDD samples.

According to the results, OP^{AA} in RDD from the 2 bituminous coal mines is markedly driven by Fe content. Huang et al. (1998) defined bioavailable Fe (BAI) in coal as the free-Fe released in a 10 mM phosphate solution, pH 4.5 which is the pH of the phagolysosomes of lung's macrophages. They hypothesised that the prevalence of CWP may be higher in coal workers exposed to coal dust with high acid-soluble Fe^{2+} and low buffering capacity (low carbonate minerals in coal) than in workers exposed to coal with low acid-soluble Fe^{2+} and high buffering capacity. Huang et al. (2005) found a high correlation (R = 0.94) of BAI values of bituminous coal with CWP cases in coal mining areas of the United States, as well as with the content of sulphate and pyrite sulphur (R = 0.91). Indeed, the low OP^{AA} for the wagon's floor dust and the lack of correlation with pyrite and Fe might be due to the low content of pyrite (0.3%) and the high buffering effect of calcite (38%) of this specific sample, although this buffering does still not account for the absence of correlation of OP^{AA} and pyrite content in the subbituminous coal samples (SSC mine). Similarly, Gilmour et al. (2004) found that high-sulphur (bituminous) coal produces more toxic RDD emissions than low-sulphur subbituminous coal and lignite. Cohn et al. (2006) suggested that the toxicity of coal dust may be in part explained by the occurrence of pyrite, and Moreno et al. (2019) reported that pyrite particles might remain for an entire year in the lungs, promoting the formation of reactive oxygen species (ROS) within cells, and potentially contributing to the pathogenesis of CWP.

The mineralogical analysis shows that the dominant mode of occurrence of Fe in the BWC, BSC and SSC RDD samples is as pyrite. Thus, using all samples from the BWC and BSC mines, with the exception of the train floor sample from the BWC mine, it can be concluded that the pyrite contents in RDD and OP^{AA} are highly correlated ($R^2 = 0.71$). Pyrite is easily oxidised into sulphuric acid and Fe-oxide, and it usually contains relevant proportions of Mn and Mo (also found to be correlated with OP^{AA}). In addition, the products of pyrite oxidation include gypsum, alunite, jarosite, tenardite, celestine and barite. Mg, Ca, Na, K, Cu, Mo, Cr, Pb, Zn, As, Ba, Rb, Sb, Cs and Sr can occur in coal within these sulphates (see Fig. 4c and d for the occurrence of Ca-Na sulphates and celestine in suspended dust from the BWC mine), as well as in other minerals such as molybdates and chromates, are correlated with OP^{AA} or OP^{GSH} and can produce oxidative reactions in the lung cells. Using other indicators Gilmour et al. (2004) also observed a contribution to toxicity from sulphates, and Schins and Borm (1999) reported that sulphates have also been suggested to play a dominant role in anti-protease inactivation. Most of the above listed elements in other types of dust have been identified as OP-relevant by Godri et al. (2011); Janssen et al. (2014); Pant et al. (2015); Moreno et al. (2017) and Soltani et al. (2018) using the same OP technique.

Titanium content is also highly correlated with OP^{GSH} (Fig. 10) for the RDD from the bituminous coal mines. This correlation increases notably for OP^{AA} if the anatase (TiO_2 analysed by XRD) is considered instead of Ti (Fig. 9). As shown in Fig. 11, the anatase and Ti contents have a low correlation ($R^2 = 0.21$) because a significant proportion of Ti probably occurs in aluminium silicate minerals substituting for other elements, whereas anatase usually occurs in very fine crystal aggregates, mostly mixed with clay mineral assemblages (Fig. 4e and f). Oberdöster et al. (1992) found that TiO_2 particles could produce significantly inflammation and interstitial translocation in the lung, with higher effects for ultrafine-TiO_2 than for the fine size fractions. Schins and Borm (1999) found also a significant role of TiO_2 for increasing 8-oxodG/dG ratios in toxicity. Hamilton et al. (2009) demonstrated that alteration of anatase TiO_2 nanomaterial into a fibre structure of greater than 15 μm creates a highly toxic particle and initiates an inflammatory response by alveolar macrophages.

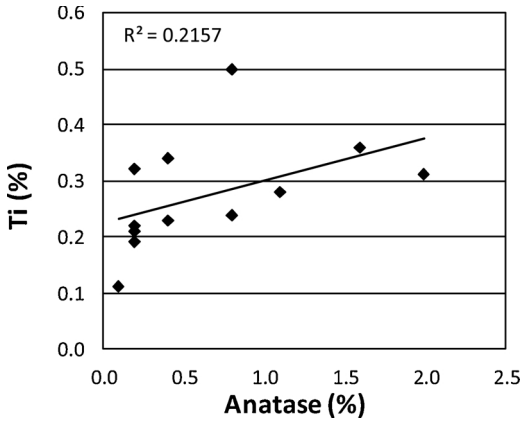

Fig. 11. Cross correlation plots of the the Ti (%) and anatase (%) contents.

Various workers have demonstrated the combined role of both size and chemical composition of dust in producing ROS (Schins and Borm, 1999; Borm, 2002; Li et al. (2003, 2008; Gilmour et al., 2004). In our study we did not find a negative correlation of Fe and size, probably because we already evaluated respirable dust with D50 close to 4 μm. Conversely, when considering the RDD but a positive size-OP^{AA} relationship was found in the multilinear regression. This might be due to the fact that, when considering this fine PM, pyrite is associated with the coal organic matrix, being enriched in the coarser sizes compared with clays.

The above evaluation of the correlation of OP with the chemical and mineralogical patterns of RDD is based on the samples from the mines working bituminous coal (BWC and BSC mines). Excluding the case of anatase, when adding the four samples from subbituminous coal (SSC samples), the correlation with Fe decreases markedly. Furthermore, the OP^{TOT} values reached for these four RDD SSC mine samples are not as high as the values seen in the bituminous coal mine samples, which might be due in part to the very high clay mineral content (24–41%db), as compared with the other RDD samples (3–28% db). In this context it has been reported that the toxicity of RCS decreases when the quartz crystals are coated with clay minerals (Pavan et al., 2019; Pavan and Fubini, 2017; Turci et al., 2015). Thus, if pyrite crystals are embedded with clay mineral aggregates or the coal matrix, then their toxicity might be decreased. As shown in Fig. 4, the SEM-EDX analysis demonstrates that the pyrite in the suspended dust from both the BWC (Fig. 4g to i) and SSC (Fig. 4j to l) mines is mostly present as isolated particles or aggregates. However, when using the SEM-EDX to analyse the samples from the coal seams (Fig. S5), it was shown that pyrite is embedded in the coal matrix in BWC mine dust, while it occurs in the clay matrix in the SSC mine. Other causes, such as the different OP, might account for the different toxicological effects.

Finally, it is important to note the low OP values obtained for the RDD sampled from the floor of the BWC mine train wagons, despite the fact that this dust has a similar mineral and chemical composition to other samples from the BWC mine with higher OP yields. One possible cause for this is the fact that this DD is quite old when compared with the other DD samples since there is evidence that the ageing of the surface of the RCS particles can decrease their toxicological effect markedly (Turci et al., 2015).

4. Conclusions

In this study, we aimed to characterize underground coal mine dust

evaluating particle sizes, mineralogical and geochemical patterns and their potential impacts on health, identifying their source origins using combined geochemical, mineralogical, and toxicological tools. We also investigated how DD finer than 500 µm in coal mines may be used to deduce the mineralogical and chemical patterns of respirable dust in the mine. We adopted a novel approach by separating the respirable component present in DD (RDD) and comparing its compositional patterns with samples of total suspended ambient PM (TSP) and PM10 (PM finer than 10 µm).

Deposited dust (DD) within coal mines contains a higher relative proportion of the finest fractions as the distance from the WFs increases, which is attributed to the fact that emissions of coarser particles are higher close to the main emission sources (WF), with only the finer fractions being transported longer distances through the galleries. Obviously, the absolute concentrations of PM2.5 and PM10 are much higher closer to the WF, but the relative contributions of the finer fraction increase with distance from the source.

In the WFs, the RDD fraction of the DD varied from up to 11–13%v in the BWC mine to 29%v in the SSC mine. At the ANC and BWC mines, we demonstrated a negative correlation between moisture in the DD and its proportion of RDD, but this same correlation was not observed in the SSC mine, possibly due to the fact that in the ANC and BWC mines, the anthracite and bituminous ranks result in lower moisture in the coal. In addition, the total moisture present might be highly influenced by water condensation, whereas in the subbituminous coal the moisture content of the dust seems to be dominated by the coal moisture, not by the condensation that may agglomerate dust.

In general, the DD mineralogy of the access gallery or WF is characterised by an ash yield when compared with its parent coal channel profile. In contrast, clay minerals tend to increase in the parent coal. AMD solutions reach the roof and walls of the galleries and give rise to the formation of sulphate minerals such as jarosite-alunite and gypsum. The dust arising from the emission of these sulphate-crusted minerals is highly loaded with potentially toxic trace metals/metalloids such as As, Pb, Zn, Sb, Cd. Gunited walls in the galleries might prevent, or at least lessen, the emission of high jarosite dust from the walls.

When compared with the parent coal, DD is enriched in a number of metals potentially associated with wear from mining machinery (Fe, Mn, V, W, Cr, Ni and Co, depending on the mine), elements associated with sulphates from AMD (Fe, As, Sb, Zn, Pb, Mn, Mg and Na, also depending on the mine), and Zn, probably due to emissions from the wear on the cylinders of the mine belts (especially in the galleries of the BSC and SSC mines).

The percentage of RCS was always higher in the vicinities of the WFs (in the cases of the SSC was higher by up to 20%) than farther away; however, when calculating the RCS on the basis of the DD (deposited dust < 500 µm), these contents were quite reduced in all mines (the highest content was 6.5% in the SSC mine).

In the case of RDD samples quartz and carbonate minerals decrease markedly (by 40%, on average) compared to DD, while the content of the other minerals is broadly similar, as demonstrated by the major element content. However, some potentially hazardous trace elements increased in RDD (As, Cd, Sb and Se).

Finally, the evaluation of the correlations of the mineral and elemental contents of RDD with the respective Oxidative Potential showed that OP^{AA} and OP^{TOT} highly correlated with Fe, Si, Mn and Ba, and Ba, Sr, Na and Ti with OP^{GSH}. The results demonstrate that Fe is the element with the highest OP^{TOT} and OP^{AA} impact in most RDD samples from the BWC and SSC mines, probably due to the oxidation of pyrite in these mines, supporting the findings by Huang et al. (1998, and 2005) on the high impact of acidic components from pyrite oxidation on the coal workers' pneumoconiosis (CWP) injuries. In the case of the SSC mine, with even higher pyrite content, the OP is much lower, probably due to the fact that pyrite occurs embedded in clay minerals or is less easily oxidised than in the other dust samples. The buffering of the acidic species by calcite is not enough to account for the low OP of these samples. A number of elements and minerals potentially arising from direct pyrite oxidation or acid mine drainage (sulphate minerals, As, Ba, Cr, Mo, Mn, Pb, Sr, Zn, among others) contributed also to increase OP values. To conclude, we found anatase (TiO_2) highly correlated with OP^{TOT} and OP^{AA} when using all samples from all mines. However, anatase and Ti contents have a low correlation (R^2 =0.21), probably due to Ti being predominantly in aluminium silicate minerals (substituting other elements), whereas anatase occurs in fine crystal aggregates in the mineral matter of dust. To conclude, we found anatase (TiO_2) highly correlated with OP^{TOT} and OP^{AA} when using all samples from all mines. However, anatase and Ti contents have a low correlation (R^2 = 0.21), probably due to Ti being predominantly in aluminium silicate minerals (substituting other elements), whereas anatase occurs in fine crystal aggregates in the mineral matter of dust.

Credits of authors

The corresponding author, Pedro Trechera, is responsible for ensuring that the descriptions are accurate and agreed by all authors, did the sampling and most of the analyses and most of writing.

Xavier Querol participated in the sampling and analysis, discussed results, also wrote some sections and reviewed the manuscript.

Zhuang Xinguo, Baoqing Li, Jing Li, Yunfei Shangguan and Patricia Córdoba, participated in the sampling of different mines, discussed results and reviewed the manuscript.

Ana Oliete and Frank Kelly did the OP analysis, wrote a section and reviewed the manuscript.

Teresa Moreno, Natalia Moreno, Konrad Kandler performed SEM and DRX analyses, discussed results and reviewed the manuscript.

Declaration of Competing Interest

The authors declare that they have no known competing financial interests or personal relationships that could have appeared to influence the work reported in this paper.

Acknowledgements

This study was supported by Generalitat de Catalunya (AGAUR 2017 SGR41), Spain; by the National Science Foundation of China (grant 41972180); the Program of Introducing Talents of Discipline to Universities (grant B14031) and Overseas Top Scholars Program for the Recruitment of Global Experts, China; the Deutsche Forschungsgemeinschaft (DFG, German Research Foundation, grant4 16816480) and by the Spanish Ministry of Science and Innovation (Excelencia Severo Ochoa, Project CEX2018-000794-S). Pedro Trechera is contracted by the ROCD (Reducing risks from Occupational exposure to Coal Dust) project supported by the European Commission Research Fund for Coal and Steel; Grant Agreement Number 754205.

Appendix A. Supplementary data

Supplementary material related to this article can be found, in the online version, at doi:https://doi.org/10.1016/j.jhazmat.2020.122935.

References

Alcobe, X., Bassa, J., Tarruella, I., Roca, A., Vinals, J., 2001. Structural characterization of synthetic Beudantite-type phases by Rietveld refinement. Mater. Sci. Forum 378–383, 671–676.

Aneja, V.P., Isherwood, A., Morgan, P., 2012. Characterization of particulate matter (PM10) related to surface coal mining operations in Appalachia. Atmos. Environ. 54, 496–501. https://doi.org/10.1016/j.atmosenv.2012.02.063.

Baker, M.A., Cerniglia, G.J., Zaman, A., 1990. Microtiter plate assay for the measurement of glutathione and glutathione disulfide in large numbers of biological samples. Anal. Biochem. 190, 360–365. https://doi.org/10.1016/0003-2697(90)90208-Q.

Borm, Pa.J.A., 1997. Toxicity and occupational health hazards of coal fly ash (CFA). A Review of Data and Comparison to Coal Mine Dust. Ann. Occup. Hyg 41. https://doi.

org/10.1093/annhyg/41.6.659.
Borm, P.J.A., 2002. Particle toxicology: from coal mining to nanotechnology. Inhal. Toxicol. 14, 311–324. https://doi.org/10.1080/08958370252809086.
Brodny, J., Tutak, M., 2018. Exposure to harmful dusts on fully powered longwall coal mines in Poland. Int. J. Environ. Res. Public Health 15, 1846. https://doi.org/10.3390/ijerph15091846.
Brown, J.S., Gordon, T., Price, O., Asgharian, B., 2013. Thoracic and respirable particle definitions for human health risk assessment. Part. Fibre Toxicol. 10, 12. https://doi.org/10.1186/1743-8977-10-12.
Calas, A., Uzu, G., Kelly, F.J., Houdier, S., Martins, J.M.F., Thomas, F., Molton, F., Charron, A., Dunster, C., Oliete, A., Jacob, V., Besombes, J.L., Chevrier, F., Jaffrezo, J.L., 2018. Comparison between five acellular oxidative potential measurement assays performed with detailed chemistry on PM10 samples from the city of Chamonix (France). Atmos. Chem. Phys. 18, 7863–7875. https://doi.org/10.5194/acp-18-7863-2018.
Castranova, V., 2000. From coal mine dust to quartz: mechanisms of pulmonary pathogenicity. Inhal. Toxicol. 12, 7–14. https://doi.org/10.1080/08958378.2000.11463226.
Chuang, H.-C., BéruBé, K., Lung, S.-C.C., Bai, K.-J., Jones, T., 2013. Investigation into the oxidative potential generated by the formation of particulate matter from incense combustion. J. Hazard. Mater. 244–245, 142–150. https://doi.org/10.1016/j.jhazmat.2012.11.034.
Chung, F.H., 1974. Quantitative interpretation of X-ray diffraction patterns of mixtures. I. Matrix-flushing method for quantitative multicomponent analysis. J. Appl. Crystallogr. 7 (6), 519–525. https://doi.org/10.1107/S0021889874010375.
Cogram, P., 2018. Jarosite. Reference Module in Earth Systems and Environmental Sciences. Elsevierhttps://doi.org/10.1016/B978-0-12-409548-9.10960-1.
Cohen, R., Patel, A., Green, F., 2008. Lung disease caused by exposure to coal mine and silica dust. Semin. Respir. Crit. Care Med. 29, 651–661. https://doi.org/10.1055/s-0028-1101275.
Cohn, C.A., Laffers, R., Simon, S.R., O'Riordan, T., Schoonen, M.A.A., 2006. Role of pyrite in formation of hydroxyl radicals in coal: possible implications for human health. Part. Fibre Toxicol. 3, 16. https://doi.org/10.1186/1743-8977-3-16.
Colinet, J.F., Rider, J.P., Listak, J.M., Organiscak, J.A., Wolfe, A.L., 2010. Best practices for dust control in coal mining. IC 9517 Inf. Circ. Best Pract. Dust Control Coal Min. 01, 17–36.
Costa, D.L., Dreher, K.L., 1997. Bioavailable transition metals in particulate matter mediate cardiopulmonary injury in healthy and compromised animal models. Environ. Health Perspect. 105, 1053–1060. https://doi.org/10.1289/ehp.97105s51053.
Dai, S., Zhou, Y., Ren, D., Wang, X., Li, D., Zhao, L., 2007. Geochemistry and mineralogy of the Late Permian coals from the Songzo Coalfield, Chongqing, southwestern China. Sci. China Ser. D Earth Sci. 50, 678–688. https://doi.org/10.1007/s11430-007-0001-4.
Dai, S., Ren, D., Zhou, Y., Chou, C.-L., Wang, X., Zhao, L., Zhu, X., 2008. Mineralogy and geochemistry of a superhigh-organic-sulfur coal, Yanshan Coalfield, Yunnan, China: evidence for a volcanic ash component and influence by submarine exhalation. Chem. Geol. 255, 182–194. https://doi.org/10.1016/J.CHEMGEO.2008.06.030.
Duarte, A.L., DaBoit, K., Oliveira, M.L.S., Teixeira, E.C., Schneider, I.L., Silva, L.F.O., 2019. Hazardous elements and amorphous nanoparticles in historical estuary coal mining area. Geosci. Front. 10, 927–939. https://doi.org/10.1016/j.gsf.2018.05.005.
Ercal, N., Gurer-Orhan, H., Aykin-Burns, N., 2001. Toxic metals and oxidative stress part I: mechanisms involved in me-tal induced oxidative damage. Curr. Top. Med. Chem. 1, 529–539.
Fabiano, B., Currò, F., Reverberi, A.P., Palazzi, E., 2014. Coal dust emissions: from environmental control to risk minimization by underground transport. An applicative case-study. Process Saf. Environ. Prot. 92, 150–159. https://doi.org/10.1016/j.psep.2013.01.002.
Font, O., Moreno, T., Querol, X., Martins, V., Sánchez Rodas, D., de Miguel, E., Capdevila, M., 2019. Origin and speciation of major and trace PM elements in the Barcelona subway system. Transp. Res. Part D Transp. Environ. 72, 17–35. https://doi.org/10.1016/j.trd.2019.03.007.
Ghio, A.J., Madden, M.C., 2017. Human lung injury following exposure to humic substances and humic-like substances. Environ. Geochem. Health 1–11. https://doi.org/10.1007/s10653-017-0008-5.
Ghose, M.K., Majee, S.R., 2007. Characteristics of hazardous airborne dust around an indian surface coal mining area. Environ. Monit. Assess. 130, 17–25. https://doi.org/10.1007/s10661-006-9448-6.
Gilmour, M.I., O'Connor, S., Dick, C.A.J., Miller, C.A., Linak, W.P., 2004. Differential pulmonary inflammation and in vitro cytotoxicity of size-fractionated fly ash particles from pulverized coal combustion. J. Air Waste Manag. Assoc. 54 (3), 286–295. https://doi.org/10.1080/10473289.2004.10470906.
Godri, K.J., Harrison, R.M., Evans, T., Baker, T., Dunster, C., Mudway, I.S., Kelly, F.J., 2011. Increased oxidative burden associated with traffic component of ambient particulate matter at roadside and urban background schools sites in London. PLoS One 7, e21961. https://doi.org/10.1371/journal.pone.0021961.
Gustafsson, Å., Krais, A.M., Gorzsás, A., Lundh, T., Gerde, P., 2018. Isolation and characterization of a respirable particle fraction from residential house-dust. Environ. Res. 161, 284–290. https://doi.org/10.1016/J.ENVRES.2017.10.049.
Haibin, L., Zhenling, L., 2010. Recycling utilization patterns of coal mining waste in China. Resour. Conserv. Recycl. 54, 1331–1340. https://doi.org/10.1016/j.resconrec.2010.05.005.
Hamilton, R.F.Jr., Wu, N., Porter, D., Buford, M., Wolfarth, M., Holian, A., 2009. Particle length-dependent titanium dioxide nanomaterials toxicity and bioactivity. Part. Fibre Toxicol. 6, 35. https://doi.org/10.1186/1743-8977-6-35.
He, J., Li, W., Liu, J., Chen, S., Frost, R.L., 2019. Investigation of mineralogical and bacteria diversity in Nanxi River affected by acid mine drainage from the closed coal mine: Implications for characterizing natural attenuation process. Spectrochim. Acta Part A Mol. Biomol. Spectrosc. 217, 263–270. https://doi.org/10.1016/J.SAA.2019.03.069.
Hendryx, M., O'Donnell, K., Horn, K., 2008. Lung cancer mortality is elevated in coal-mining areas of Appalachia. Lung Cancer 62, 1–7. https://doi.org/10.1016/j.lungcan.2008.02.004.
Huang, X., Fournier, J., Koenig, K., Chen, L.C., 1998. Buffering capacity of coal and its acid-soluble Fe^{2+} content: possible role in coal workers' pneumoconiosis. Chem. Res. Toxicol. 11, 722–729. https://doi.org/10.1021/tx970151o.
Huang, X., Li, W., Attfield, M.D., Nádas, A., Frenkel, K., Finkelman, R.B., 2005. Mapping and prediction of Coal Workers' Pneumoconiosis with bioavailable iron content in the bituminous coals. Environ. Health Perspect. 113, 964–968. https://doi.org/10.1289/ehp.7679.
Hudson-Edwards, K.A., Smith, A.M.L.D., Bennett, A.J., Murphy, P.J., Wright, K., 2008. Comparison of the structures of natural and synthetic Pb-Cu-jarosite-type compounds. Eur. J. Mineral. 20, 241–252. https://doi.org/10.1127/0935-1221/2008/0020-1788.
Iriyama, K., Yoshiura, M., Iwamoto, T., Ozaki, Y., 1984. Simultaneous determination of uric and ascorbic acids in human serum by reversed-phase high-performance liquid chromatography with electrochemical detection. Anal. Biochem. 141, 238–243. https://doi.org/10.1016/0003-2697(84)90451-2.
Janssen, N.A.H., Yang, A., Strak, M., Steenhof, M., Hellack, B., Gerlofs-Nijland, M.E., Kuhlbusch, T., Kelly, F., Harrison, R., Brunekreef, B., Hoek, G., Cassee, F., 2014. Oxidative potential of particulate matter collected at sites withdifferent source characteristics. Sci. Total Environ. 472, 572–581. https://doi.org/10.1016/j.scitotenv.2013.11.099.
Jiang, X., Lu, W.X., Zhao, H.Q., Yang, Q.C., Yang, Z.P., 2014. Potential ecological risk assessment and prediction of soil heavy-metal pollution around coal gangue dump. Nat. Hazards Earth Syst. Sci. Discuss. 14, 1599–1610. https://doi.org/10.5194/nhess-14-1599-2014.
Johann-Essex, V., Keles, C., Rezaee, M., Scaggs-Witte, M., Sarver, E., 2017. Respirable coal mine dust characteristics in samples collected in central and northern Appalachia. Int. J. Coal Geol. 182, 85–93. https://doi.org/10.1016/J.COAL.2017.09.010.
Kadiiska, M.B., Mason, R.P., Dreher, K.L., Costa, D.L., Ghio, A.J., 1997. In vivo evidence of free radical formation in the rat lung after exposure to an emission source air pollution particle †. Chem. Res. Toxicol. 10, 1104–1108. https://doi.org/10.1021/tx970049r.
Kelly, F.J., 2003. Oxidative stress: its role in air pollution and adverse health effects. Occup. Environ. Med. 60, 612–616. https://doi.org/10.1136/oem.60.8.612.
Kerolli–Mustafa, M., Fajković, H., Ronèević, S., Ćurković, L., 2015. Assessment of metal risks from different depths of jarosite tailing waste of Trepça Zinc Industry, Kosovo based on BCR procedure. J. Geochemical Explor. 148, 161–168. https://doi.org/10.1016/J.GEXPLO.2014.09.001.
Ketris, M.P., Yudovich, Y.E., 2009. Estimations of Clarkes for Carbonaceous biolithes: world averages for trace element contents in black shales and coals. Int. J. Coal Geol. 78, 135–148. https://doi.org/10.1016/J.COAL.2009.01.002.
Kim, A.G., 2004. Locating fires in abandoned underground coal mines. Int. J. Coal Geol. 59, 49–62. https://doi.org/10.1016/j.coal.2003.11.003.
Kolitsch, U., Pring, A., 2001. Crystal chemistry of the crandallite, beudantite and alunite groups: a review and evaluation of the suitability as storage materials for toxic metals. J. Mineral. Petrol. Sci. 96, 67–78. https://doi.org/10.2465/jmps.96.67.
Li, N., Sioutas, C., Cho, A., Schmitz, D., Misra, C., Sempf, J., Wang, M., Oberley, T., Froines, J., Nel, A., 2003. Ultrafine particulate pollutants induce oxidative stress and mitochondrial damage. Environ. Health Perspect. 111, 455–460. https://doi.org/10.1289/ehp.6000.
Li, N., Xia, T., Nel, A.E., 2008. The role of oxidative stress in ambient particulate matter-induced lung diseases and its implications in the toxicity of engineered nanoparticles. Free Radical Bio Med. 44, 1689–1699. https://doi.org/10.1016/j.freeradbiomed.2008.01.028.
Li, H., Ji, H., Shi, C., Gao, Y., Zhang, Y., Xu, X., Ding, H., Tang, L., Xing, Y., 2017. Distribution of heavy metals and metalloids in bulk and particle size fractions of soils from coal-mine brownfield and implications on human health. Chemosphere 172, 505–515. https://doi.org/10.1016/J.CHEMOSPHERE.2017.01.021.
Li, S., Xie, B., Hu, S., Jin, H., Liu, H., Tan, X., Zhou, F., 2019. Removal of dust produced in the roadway of coal mine using a mining dust filtration system. Adv. Powder Technol. 30, 911–919. https://doi.org/10.1016/J.APT.2019.02.005.
Liang, Y., Wong, O., Yang, L., Li, T., Su, Z., 2006. The development and regulation of occupational exposure limits in China. Regul. Toxicol. Pharmacol. 46, 107–113. https://doi.org/10.1016/j.yrtph.2006.02.007.
Madzivire, G., Maleka, R.M., Tekere, M., Petrik, L.F., 2019. Cradle to cradle solution to problematic waste materials from mine and coal power station: acid mine drainage, coal fly ash and carbon dioxide. J. Water Process Eng. 30, 100474. https://doi.org/10.1016/j.jwpe.2017.08.012.
Mohanty, A.K., Lingaswamy, M., Rao, V.G., Sankaran, S., 2018. Impact of acid mine drainage and hydrogeochemical studies in a part of Rajrappa coal mining area of Ramgarh District, Jharkhand State of India. Groundw. Sustain. Dev. 7, 164–175. https://doi.org/10.1016/J.GSD.2018.05.005.
Moreno, T., Higueras, P., Jones, T., McDonald, I., Gibbons, W., 2005. Size fractionation in mercury-bearing airborne particles (HgPM10) at Almadén, Spain: implications for inhalation hazards around old mines. Atmos. Environ. 39, 6409–6419. https://doi.org/10.1016/j.atmosenv.2005.07.024.
Moreno, T., Martins, V., Querol, X., Jones, T., BéruBé, K., Minguillón, M.C., Amato, F., Capdevila, M., de Miguel, E., Centelles, S., Gibbons, W., 2015. A new look at inhalable metalliferous airborne particles on rail subway platforms. Sci. Total Environ.

505, 367–375. https://doi.org/10.1016/J.SCITOTENV.2014.10.013.
Moreno, T., Kelly, F.J., Dunster, C., Oliete, A., Martins, V., Reche, C., Minguillón, M.C., Amato, F., Capdevila, M., de Miguel, E., Querol, X., 2017. Oxidative potential of subway PM2.5. Atmos. Environ. 148, 230–238. https://doi.org/10.1016/J.ATMOSENV.2016.10.045.
Moreno, T., Trechera, P., Querol, X., Lah, R., Johnson, D., Wrana, A., Williamson, B., 2019. Trace element fractionation between PM10 and PM2.5 in coal mine dust: implications for occupational respiratory health. Int. J. Coal Geol. 203, 52–59. https://doi.org/10.1016/j.coal.2019.01.006.
Murphy, P.J., Smith, A.M.L., Hudson-Edwards, K.A., Dubbin, W.E., Wright, K., 2009. Raman and IR spectroscopic studies of Alunite-supergroup compounds containing Al, Cr^{3+}, Fe^{3+} and V^{3+} at the B Site. Can. Mineral. 47, 663–681. https://doi.org/10.3749/canmin.47.3.663.
Niosh, 2002. Health effects of occupational exposure to respirable crystalline silica. DHHS Publ. No. 2002-129 145, 127 https://doi.org/2002-129.
O'Keefe, J.M.K., Henke, K.R., Hower, J.C., Engle, M.A., Stracher, G.B., Stucker, J.D., Drew, J.W., Staggs, W.D., Murray, T.M., Hammond, M.L., Adkins, K.D., Mullins, B.J., Lemley, E.W., 2010. CO_2, CO, and Hg emissions from the Truman Shepherd and Ruth Mullins coal fires, eastern Kentucky. USA. Sci. Total Environ. 408, 1628–1633. https://doi.org/10.1016/J.SCITOTENV.2009.12.005.
Oberdöster, G., Ferin, J., Lehnert, B.E., 1992. Correlation between particle size, in vivo particle persistence, and lung injury. Environ. Health Perspect. 102, 173–179. https://doi.org/10.1289/ehp.102-1567252.
Pallarés, J., Herce, C., Bartolomé, C., Peña, B., 2017. Investigation on co-firing of coal mine waste residues in pulverized coal combustion systems. Energy 140, 58–68. https://doi.org/10.1016/J.ENERGY.2017.07.174.
Pant, P., Baker, S.J., Shukla, A., Maikawa, C., Godri Pollit, K.J., Harrison, R.M., 2015. The PM10 fraction of road dust in the UK and India: characterization, source profiles and oxidative potential. Sci. Total Environ. 530-531, 445–452. https://doi.org/10.1016/j.scitotenv.2015.05.084.
Patra, A.K., Gautam, S., Kumar, P., 2016. Emissions and human health impact of particulate matter from surface mining operation-A review. Environ. Technol. Innov. 5, 233–249. https://doi.org/10.1016/j.eti.2016.04.002.
Pavan, C., Fubini, B., 2017. Unveiling the variability of "Quartz hazard" in light of recent toxicological findings. Chem. Res. Toxicol. 30, 469–485. https://doi.org/10.1021/acs.chemrestox.6b00409.
Pavan, C., Delle Piane, M., Gullo, M., Filippi, F., Fubini, B., Hoet, P., Horwell, C.J., Huaux, F., Lison, D., Lo Giudice, C., Martra, G., Montfort, E., Schins, R., Sulpizi, M., Wegner, K., Wyart-Remy, M., Ziemann, C., Turci, F., 2019. The puzzling issue of silica toxicity: are silanols bridging the gaps between surface states and pathogenicity? Part. Fibre Toxicol. 16, 32. https://doi.org/10.1186/s12989-019-0315-3.
Petavratzi, E., Kingman, S., Lowndes, I., 2005. Particulates from mining operations: a review of sources, effects and regulations. Miner. Eng. 18, 1183–1199. https://doi.org/10.1016/j.mineng.2005.06.017.
Querol, X., 1993. The Occurrence and Distribution of Trace Elements in the Teruel Mining District Coals and Their Behaviour During Coal Combustion. European Coal and Steel Community Project 7220/ED/014.
Querol, X., Whateley, M.K.G., Fernández-Turiel, J.L., Tuncali, E., 1997. Geological controls on the mineralogy and geochemistry of the Beypazari lignite, central Anatolia. Turkey. Int. J. Coal Geol. 33, 255–271. https://doi.org/10.1016/S0166-5162(96)00044-4.
Querol, X., Izquierdo, M., Monfort, E., Alvarez, E., Font, O., Moreno, T., Alastuey, A., Zhuang, X., Lu, W., Wang, Y., 2008. Environmental characterization of burnt coal gangue banks at Yangquan, Shanxi Province. China. Int. J. Coal Geol. 75, 93–104. https://doi.org/10.1016/J.COAL.2008.04.003.
Querol, X., Zhuang, X., Font, O., Izquierdo, M., Alastuey, A., Castro, I., van Drooge, B.L., Moreno, T., Grimalt, J.O., Elvira, J., Cabañas, M., Bartroli, R., Hower, J.C., Ayora, C., Plana, F., López-Soler, A., 2011. Influence of soil cover on reducing the environmental impact of spontaneous coal combustion in coal waste gobs: a review and new experimental data. Int. J. Coal Geol. 85, 2–22. https://doi.org/10.1016/j.coal.2010.09.002.
Rout, T.K., Masto, R.E., Padhy, P.K., George, J., Ram, L.C., Maity, S., 2014. Dust fall and elemental flux in a coal mining area. J. Geochemical Explor. 144, 443–455. https://doi.org/10.1016/J.GEXPLO.2014.04.003.
Sarver, E., Keles, C., Rezaee, M., 2019. Beyond conventional metrics: comprehensive characterization of respirable coal mine dust. Int. J. Coal Geol. 207, 84–95. https://doi.org/10.1016/j.coal.2019.03.015.
Schins, R.P.F., Borm, Pa.J.A., 1999. Mechanisms and mediators in coal dust InducedToxicity: a review. Ann. Occup. Hyg. 43, 7–33. https://doi.org/10.1016/S0003-4878(98)00069-6.
Smith, A.M.L., Hudson-Edwards, K.A., Dubbin, W.E., Wright, K., 2006. Dissolution of jarosite [KFe3(SO4)2(OH)6] at pH 2 and 8: insights from batch experiments and computational modelling. Geochim. Cosmochim. Acta 70, 608–621. https://doi.org/10.1016/J.GCA.2005.09.024.
Soltani, N., Keshavarzi, B., Sorooshian, A., Moore, F., Dunster, C., Dominguez, A.O., Kelly, F.J., Dhakal, P., Ahmadi, M.R., Asadi, S., 2018. Oxidative potential (OP) and mineralogy of iron ore particulate matter at the Gol-E-Gohar Mining and Industrial Facility (Iran). Environ. Geochem. Health 40, 1785–1802. https://doi.org/10.1007/s10653-017-9926-5.
Sperazza, M., Moore, J.N., Hendrix, M.S., 2004. High-resolution particle size analysis of naturally occurring very fine-grained sediment through laser diffractometry. J. Sediment. Res. A Sediment. Petrol. Process. 74, 736–743. https://doi.org/10.1306/031104740736.
Tang, Z., Chai, M., Cheng, J., Jin, J., Yang, Y., Nie, Z., Huang, Q., Li, Y., 2017. Contamination and health risks of heavy metals in street dust from a coal-mining city in eastern China. Ecotoxicol. Environ. Saf. 138, 83–91. https://doi.org/10.1016/j.ecoenv.2016.11.003.
Turci, F., Pavan, C., Leinardi, R., Tomatis, M., Pastero, L., Garry, D., Anguissola, S., Lison, D., Fubini, B., 2015. Revisiting the paradigm of silica pathogenicity with synthetic quartz crystals: the role of crystallinity and surface disorder. Part. Fibre Toxicol. 13, 32. https://doi.org/10.1186/s12989-016-0136-6.
Valko, M., Jomova, K., Rhodes, C.J., Kuča, K., Musílek, K., 2016. Redox- and non-redox-metal-induced formation of free radicals and their role in human disease. Arch. Toxicol. https://doi.org/10.1007/s00204-015-1579-5.
Visser, G.T., 1992. A wind-tunnel study of the dust emissions from the continuous dumping of coal. Atmos. Environ. Part A. Gen. Top. 26, 1453–1460. https://doi.org/10.1016/0960-1686(92)90130-D.
Welch, S.A., Kirste, D., Christy, A.G., Beavis, F.R., Beavis, S.G., 2008. Jarosite dissolution II—reaction kinetics, stoichiometry and acid flux. Chem. Geol. 254, 73–86. https://doi.org/10.1016/j.chemgeo.2008.06.010.